POLITECNICO
MILANO 1863

SCUOLA DI INGEGNERIA INDUSTRIALE
E DELL'INFORMAZIONE

Double-Stage PV System with Synthetic Inertia: Analysis of the Interactions between Converters

MASTER THESIS IN
ELECTRICAL ENGINEERING

Author: **Adam Pezzuolo**

Student ID:	10463421
Advisor:	Roberto Perini
Academic Year:	2020-21

Abstract

This study analyzes the model of the PV panel and DC-DC converter's control and their effects on the synthetic inertia in a double-stage conversion system (DC-DC boost converter and DC-AC inverter) employed for the connection of a PV generator to an isolated microgrid, where primary frequency regulation is carried out by rotating machines with low starting time.

The goal of the analysis is to analyze the interaction between the conversion stages DC-DC and DC-AC in the event of a power load variation, as well as their effect on synthetic inertia and other desired outputs of the system, such as frequency and working point of PV panels.

The study will be carried out analytically, finding the mathematical differential equations of all the components in the microgrid and the corresponding transfer functions, obtained by linearization and small signal analysis. Then, using the extracted model, the transfer function of desired outputs, such as grid frequency, will be calculated.

Key-words: "Synthetic Inertia Control", "Double-Stage PV System", "DC/DC Converter Control", "MPPT", "Inverter Control".

Abstract in lingua italiana

Questo studio analizza il modello del pannello fotovoltaico e del controllo del convertitore DC-DC e i loro effetti sull'inerzia sintetica in un sistema di conversione a doppio stadio (convertitore booster DC-DC più inverter DC-AC), utilizzato per il collegamento di un generatore FV a una micro-rete isolata, dove la regolazione della frequenza primaria viene effettuata dalle macchine rotanti con tempo di avviamento veloce.

L'obiettivo dell'analisi è valutare l'interazione tra gli stadi di conversione DC-DC e DC-AC in seguito ad una variazione della potenza del carico nonché il loro impatto sull'inerzia sintetica e le altre uscite del sistema, come la frequenza e il punto di lavoro dei pannelli fotovoltaici.

Lo studio sarà condotto analiticamente, trovando le equazioni differenziali di tutti i componenti della micro-rete e le corrispondenti funzioni di trasferimento, ottenute mediante linearizzazione e analisi di piccolo segnale. Successivamente, utilizzando il modello ricavato, verrà calcolata la funzione di trasferimento delle uscite desiderate, come la frequenza di rete.

Parole chiave: "Inerzia Sintetica", "Sistema Fotovoltaico", "Controllo Convertitore DC/DC", "MPPT", "Controllo Inverter".

Contents

1. Chapter one

Introduction

Wind and solar energy will play a central role in the decarbonization of the European electricity generation system as they represent a promising solution to address global warming and hydrocarbon fuel scarcity. Considering the observed growth rate, decreasing costs and the political support schemes, wind and solar PV will most likely constitute a high share of the power supply system.

Today's electricity system is based on a centralized supply in proximity to load centers and the different power plant types are designed to follow the hourly load. International transmission of electricity and storage only play a minor role. This changes significantly in energy systems with high shares of renewable energy and entails major integration challenges for the power system, such as the connection of remote sites of high variable renewable energies and their low reliability, occurring overproduction, etc. [1]. Furthermore, the inverter-based distributed generations (DGs) such as photovoltaic (PV) do not have rotating masses and grid-forming abilities, which make the micro-grid become low-inertia, weak and difficult to control, particularly in the stand-alone mode. Inertia stands for the sensitivity of frequency to the mismatch between supply and demand, therefore changes in generation or load can cause large frequency deviations and possibly leading to system instability. Moreover, PV systems are typically operated in maximum power point tracking (MPPT) mode, which emphasizes high energy usage efficiency but may cause more serious frequency events when the maximum available PV generation is higher than the demand [2].

Present day grid codes impose technical requirements to DG stations, such as the provision of frequency response. Many solutions have been proposed in the literature. Ref. [2] studies a double-stage PV plant and realizes synthetic inertia control (SIC) by charging/discharging a DC-Bus capacitor and adjusting the PV generation when it is feasible and/or necessary. However, instead of using a MPPT algorithm, a proportional-integral controller was chosen for the DC/DC boost converter. Ref [3] studied the effects on SIC of a PV generator with a double-stage conversion system connected to an isolated microgrid where primary frequency regulation is carried out by traditional rotating machines. However,

Virtual synchronous generator control (VSG) is a technique used to allow PV systems to provide inertial response of frequency, where the dynamic of a DC-link capacitor is used to mimic the dynamic of a SG's rotor [2]. [3] studied the effects on synthetic inertia response of a PV generator with a double-stage conversion system (dc-dc boost plus dc-ac inverter) connected to an isolated microgrid where primary frequency regulation is carried out by traditional rotating machines. This paper will take a step further from what has been analyzed in [3] by considering a larger PV system with faster voltage response and an external grid formed by a number of small-size SGs connected in parallel which give rise to a smaller starting time and therefore faster frequency transients.

1.1 PV Plant Topology and Control Architecture

The system is configured in a double-stage topology where the PV array is connected to a DC-DC boost converter followed by a DC/AC inverter as shown in Figure 1.1. The single-stage configuration with just a DC/AC inverter can be an alternative as it reaches higher energy efficiency rates. However, the double-stage configuration is preferred because of the following advantages: higher DC-bus voltage stability, lower total harmonic distortion (THD) on the AC side, better MPPT accuracy and simpler control scheme [4].

Consider the general scheme of Figure 1.1 for a double-stage photovoltaic unit: the external Phase Locked Loop (PLL) acquires a set of uncontrolled three-phase voltages in correspondence to the Point of Common Connection (PCC) with the external grid. The PLL defines the angle θ used for the Park transform and allows to maintain synchrony between the converter control and the external grid.

The regulation of the DC voltage and of the injected active and reactive powers is done by linear controllers. The DC bus controller generates a reference for the current control which, in turn, regulates the power injection. As regards the reactive power, the reference signal can be considered as an independent input or can be generated from an external reactive-support algorithm. In this case the reference value is zero.

A Maximum Power Point Tracking (MPPT) algorithm is also included, operating on the duty cycle of the DC boost converter. This allows for the introduction of an additional degree of freedom as it allows the DC-Bus voltage reference to not be defined by other sub-controls and can be exploited for inertia regulation. The following section is dedicated to the description of the MPPT technique used in this case study.

1.2 Incremental Conductance Technique for MPPT

The V-I characteristic of a PV module is nonlinear Figure 1.2. The power output depends on the irradiation, the temperature, and electric loading conditions, namely voltage and current at its terminals.

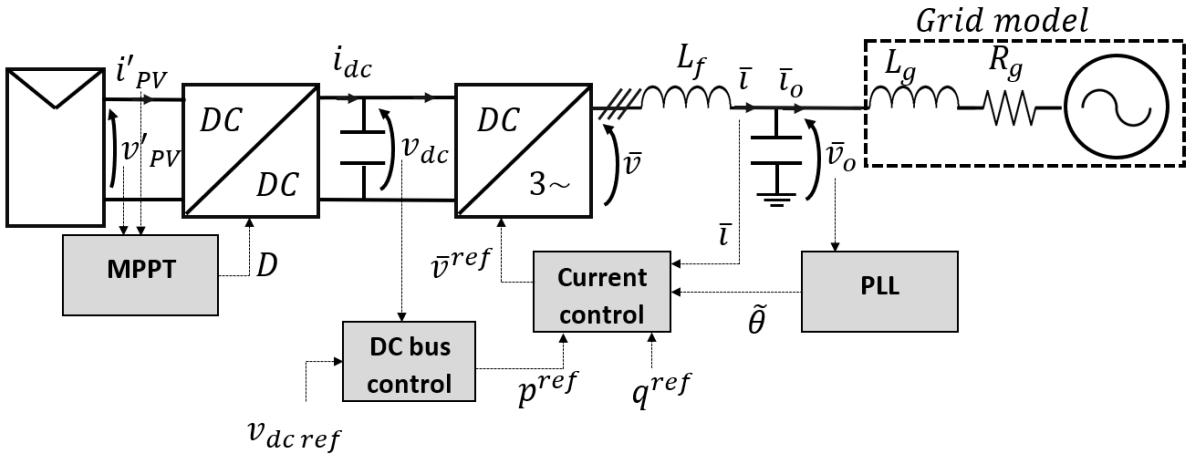

Figure 1.1 – Overall structure of a double-stage photovoltaic unit control system [5].

In general, there is a unique point on the V-I or V-P curve, called the Maximum Power Point (MPP), at which the PV system operates with maximum efficiency and produces its maximum output power according to the environmental conditions. To follow the inevitable movements of the MPP over time, many MPPT techniques have been proposed in the literature; the two most frequently discussed MPPT algorithms are the perturb-and-observe (P&O) and the incremental conductance (INC). These methods are based on the fact that on the voltage–power characteristic, the variation of the power with respect to voltage is positive (dP/dV > 0) on the left-hand side of the MPP, while it is negative (dP/dV < 0) on the right-hand side of the MPP. The main advantages of these methods are that they are suitable for any PV array, they work reasonably well under most condition and they are simple to implement on a digital controller. A detailed literature review today would lead to the conclusion that although the INC is slightly more complicated to implement, it provides better performance than P&O under both static and dynamic conditions. The two main problems of the P&O that are frequently mentioned in the literature are the oscillations around the MPP under steady-state conditions and the poor tracking (possibly in the wrong direction, away from MPP) under changing irradiance [6]. The INC method has been chosen for this study and will be briefly discussed.

Assuming v_{pv}, i_{pv} and p_{pv} are respectively voltage, current and power of the PV panel at its terminals, (1.1) calculates dp_{pv}/dv_{pv}:

$$\frac{dp_{pv}}{dv_{pv}} = \frac{d(v_{pv}i_{pv})}{dv_{pv}} = i_{pv} + v_{pv}\frac{di_{pv}}{dv_{pv}} \tag{1.1}$$

Rewriting (1.1) at MPP, gives (1.2):

$$\frac{i_{pv}}{v_{pv}} + \frac{di_{pv}}{dv_{pv}} = 0 \tag{1.2}$$

Where i_{pv}/v_{pv} is the instantaneous conductance and di_{pv}/dv_{pv} is the incremental conductance. These two quantities are used to determine the reference voltage V_{ref} as shown in the flow chart (Figure 1.5) given v_{pv}, i_{pv} as inputs for the MPPT algorithm. When the MPP is achieved V_{ref} must be equal to V_{mpp} at that instant and once it happens, the operation is maintained at MPP until a change ΔI occurs.

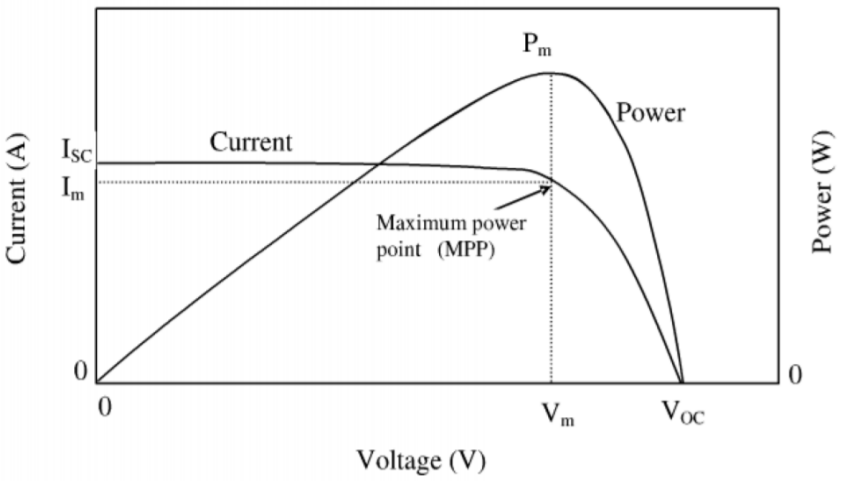

Figure 1.2 – P-V and I-V curve of a general PV source [6].

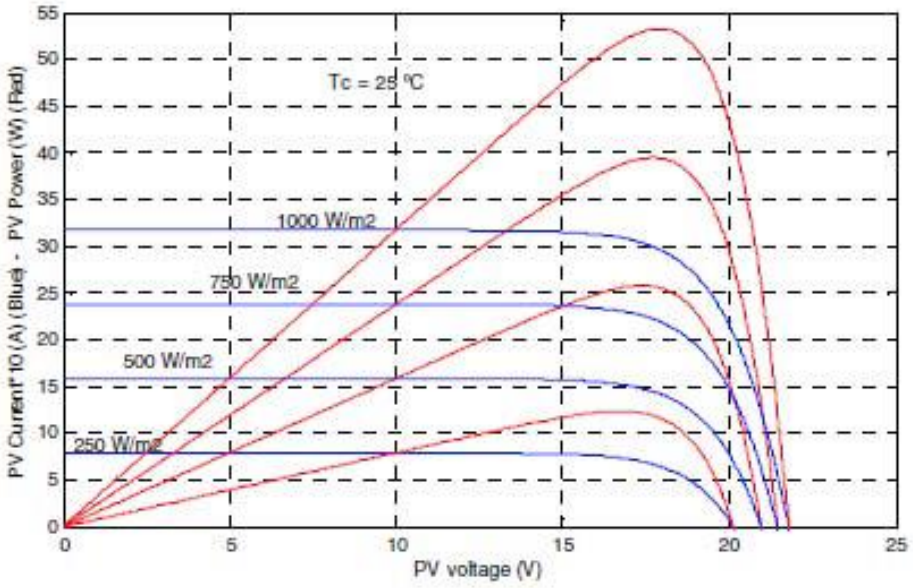

Figure 1.3 – P-V and V-I curves of a PV module for different radiation levels at constant cell temperature [7]

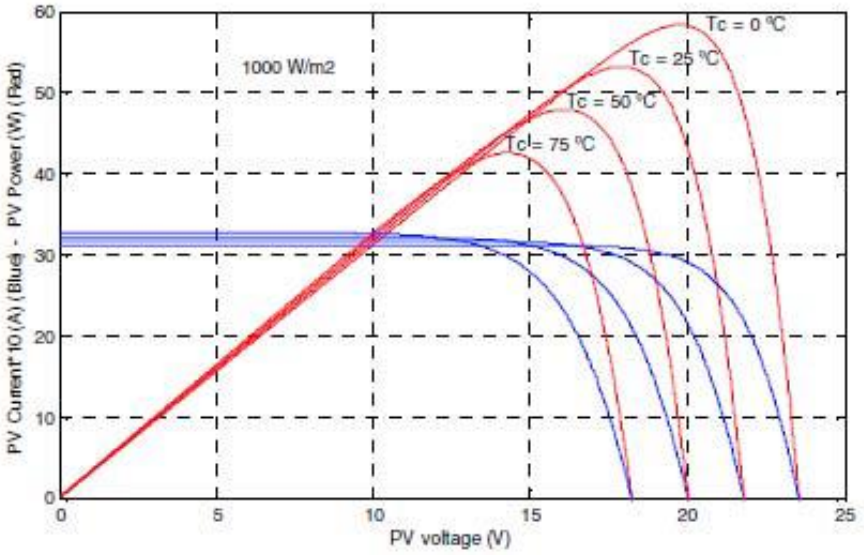

Figure 1.4 – P-V and V-I curves of a PV module for different cell temperatures at constant radiation level [7]

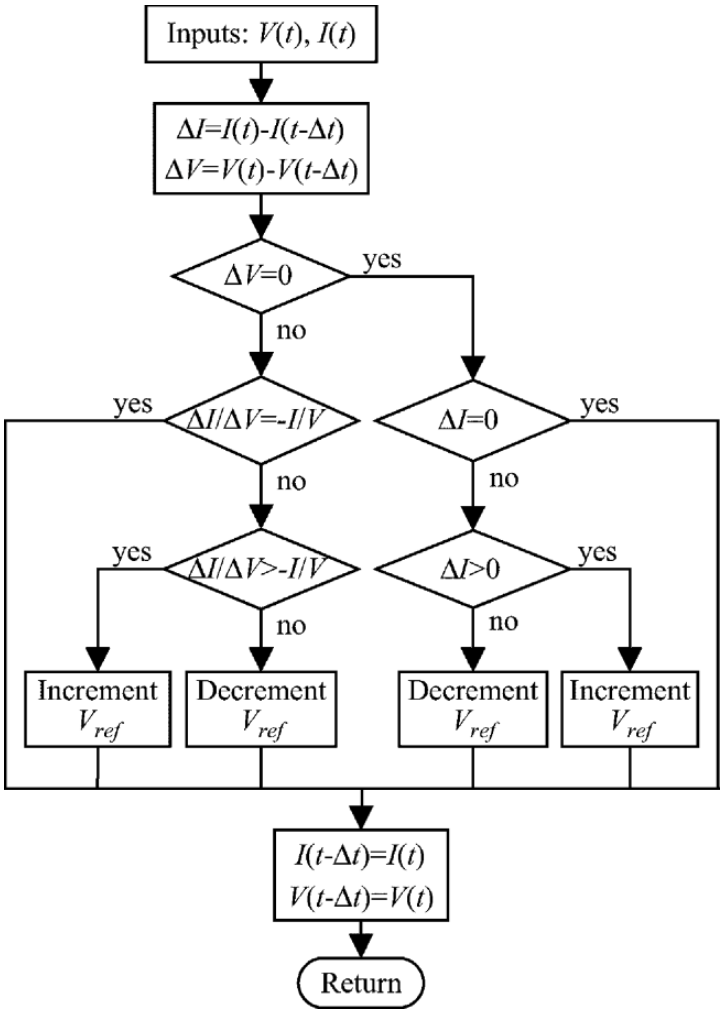

Figure 1.5 – Flow chart of Incremental Conductance method [7]

2. Chapter two

Mathematical Model of the System

This chapter deals with the mathematical modeling of the system using differential equations to derive the small signal model around the working point. In the first part, the general topology and the main ratings are illustrated; in the second part, the small signal model and the transfer function block diagram of the system are deduced, allowing to find the desired outputs through an analytical approach.

2.1 Case Study Definition

The general system topology together with its related control blocks are shown in Figure 2.1. In the presented topology, the PV generation part has the possibility of paralleling more than one string of PV panels for the case that the generation power is higher than 100 kW. In that case, each PV panel string is connected to the DC-Bus through a DC/DC converter which performs the dedicated MPPT control. A DC/AC inverter connects the DC side to the AC side. To represent the general case study, the scheme includes a filter stage and a transformer (in case the connected grid is a medium voltage grid). Finally, the grid supporting unit (GSU) and the uncontrolled units are implemented in the model to emulate the behavior of an external grid.

In this study, one single PV array is employed consisting of n_s modules connected in series, forming a string, and n_p strings connected in parallel; n_s, n_p are chosen in such a way to obtain the desired values of rated power and rated voltage of the PV-Bus. The PV-Bus capacitance C_{in} operate as a filter, damping the voltage ripple introduced by the converter. The DC-Bus capacitance C_{dc} is put in place as an energy buffer for inertia provision during frequency transients as well as for DC-Bus voltage stabilization.

The DC/AC inverter connects the system to the grid and performs the inertia provision during frequency transients by reducing/increasing the DC-Bus voltage according to its control scheme. The effects of SIC on a similar system have been studied in [3], however, due to the lower nominal power of the system, the PV-Bus voltage transients were governed by a much smaller time constant compared to that of the external grid. This implies that the effects of a frequency transient were never perceived by the PV-Bus, thus the operating point of the PV generator was never influenced. In this case study, given the larger scale of the system, the time constant that governs the PV-Bus voltage dynamic is larger, therefore voltage variations caused by MPPT control are slower. Moreover, the external grid taken in consideration has a smaller starting time than that studied in [3].

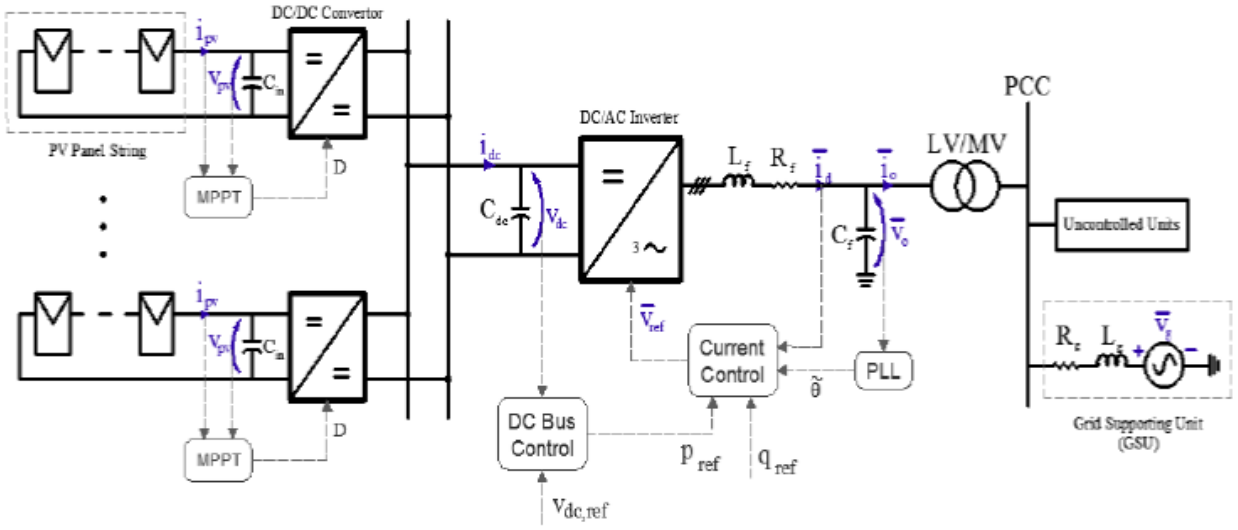

Figure 2.1 – Overall topology of the system [3].

Assuming it is formed by a number n of parallel-connected synchronous generators with rated power P_h and starting time T_{ah}, the equivalent starting time of the GSU T_{a-eq} is equal to the weighted average of the starting times of all SGs with respect to their rated power [8]:

$$T_{a-eq} = \frac{\sum_h T_{ah} \cdot P_h}{\sum_h P_h} \tag{2.1}$$

In the case of many synchronous generators of small size (50÷100kVA), this can lead to an external GSU with small starting time (50ms) that allows for faster frequency transients. From now on the equivalent starting time of the external GSU will be indicated simply as T_a.

The main ratings of the system are summarized in Table 1.

Table 1 – Main ratings of the system

PV Module Static Parameters		DC/AC Inverter Ratings	
Rated Power per module, P_{pv-mod}	305 W	Rated Power, P_{dc}	500 kW
MPP Voltage, V_{mpp}	54.7 V	Switching Frequency, f_{sw}	4 kHz
Number of modules in series, n_s	11	AC-Side Rated Voltage, V_{ac}	530 V
Number of strings in parallel, n_p	149	DC-Bus Rated Voltage, V_{dc}	$\sqrt{2}\,V_{ac}$

PV-Bus Ratings		DC/DC Converter Ratings	
Rated Power, P_{pv}	500 kW	Switching Frequency, f_{sw}	4 kHz
Rated Voltage, V_{pv}	602 V	Rated Power, P_{boost}	500 kW

External Grid		Grid Supporting Unit	
Rated Voltage, V_n	15 kV	Equivalent Starting Time, T_{a_eq}	50 ms
Grid Frequency, f_n	50 Hz	Time Delay of Primary Regulation, τ	50 ms
Rated Power, P_b	1 MVA	Regulating Energy, K_{reg}	40 p.u.

2.2 PV Source Model

Typically, for PV array modeling and system analysis, a static single-diode circuit model such as the one indicated in Figure 2.2Figure 2.2 is considered. The static PV terminal voltage V_{pv} and current I_{pv} are related by the following nonlinear relationship [9]:

$$I_{pv} = I_{ph} - I_d - \left(\frac{V_{pv} + I_{pv}R_s}{R_{sh}}\right) \tag{2.2}$$

$$I_d = I_s\left[exp\left(\frac{V_{pv} + I_{pv}R_s}{\eta n_c V_t}\right)\right] \tag{2.3}$$

Where:

I_{ph}= photo-generated PV current;
I_d= PV diode's forward-bias current;
I_s= dark saturation current;
R_s, R_{sh}= series and shunt static resistances;
n_c= number of PV cells in series in a module;
V_t= thermal voltage.
Numerical values are reported in Table 2.

The static PV model however, is not directly applicable for the dynamic analysis, therefore a linear dynamic model is presented in the following section.

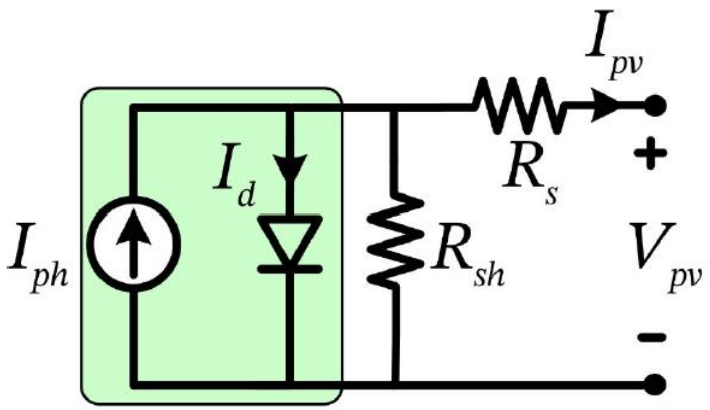

Figure 2.2 – Static nonlinear model of the PV source [9].

2.2.1 Dynamic Linear Model

The physical semiconductor structure of the PV module inherently carries a diffusion capacitance C_d due to the forward biased silicon semiconductor junction of the PV cells, and an equivalent series inductance L_s caused by the metalized bus bars interconnecting the n_c PV cells in series. The linearized dynamic model of PV source is illustrated in Figure 2.3.

The equivalent impedance in the Laplace domain can be written as follows:

$$Z_{pv-mod}(s) = (R_s + L_s) + \left(r_d // R_{sh} // \frac{1}{sC_d}\right) = (R_s + s\,L_s) + \left(\frac{R_p}{1 + sR_pC_d}\right) = \frac{(R_s + s\,L_s)(1 + sR_pC_d) + R_p}{1 + sR_pC_d} \quad (2.4)$$

Where $R_p = \frac{r_d R_{sh}}{r_d + R_{sh}}$, and by considering $R_{pv} = R_s + R_p$, equation (2.4) can be rewritten as (2.5):

$$Z_{pv\_mod}(s) = R_{pv}\frac{1 + \frac{2\xi}{\omega_z}s + \frac{s^2}{{\omega_z}^2}}{1 + \frac{s}{\omega_p}} \quad (2.5)$$

The PV impedance has a first order pole ω_p constituted by the parallel RC-network, a second order zero ω_z constituted by the interaction of parallel RC-network with the series-RL network, and a damping factor ξ.

$$\omega_p = \frac{1}{R_pC_d}$$
$$\omega_z = \frac{1}{\sqrt{L_sC_d}}\sqrt{1 + \frac{R_s}{R_p}} \quad (2.6)$$
$$\xi = \frac{1}{2}\frac{L_s + R_pR_sC_d}{\sqrt{R_pR_{pv}L_sC_d}}$$

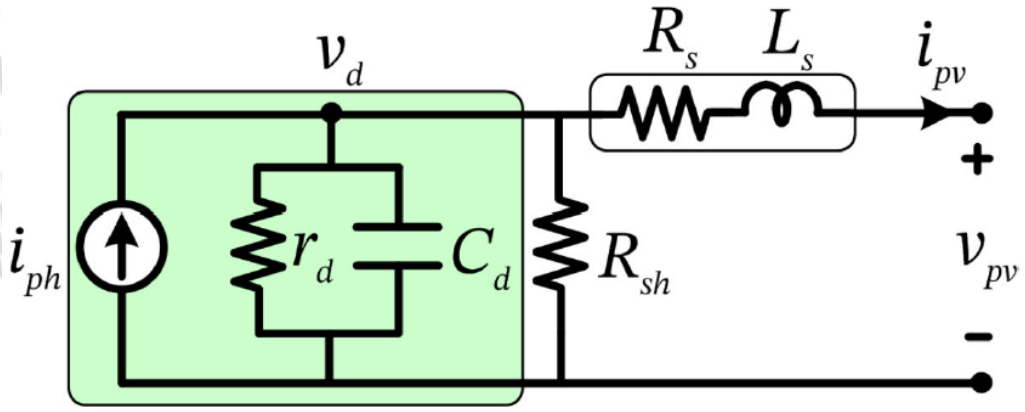

Figure 2.3 – Dynamic linear model of the PV source for small-signal analysis [9].

The effect of scaling modules in series/parallel for an array formation is shown in the following expressions. Considering equation (2.4), n_s identical modules connected in series results in (2.7):

$$Z_{pv-series} = n_s R_s\left(1+\frac{sn_sL_s}{n_sR_s}\right)+\frac{n_sR_p}{1+sn_sR_p\cdot C_d/n_s} = n_s\left[R_s\left(1+\frac{sL_s}{R_s}\right)+\frac{R_p}{1+sR_pC_d}\right] = n_sZ_{pv}. \quad (2.7)$$

Similarly, for n_p identical modules connected in parallel it results (2.8):

$$Z_{pv-parallel} = \frac{R_s}{n_p}\left(1+\frac{s\,L_s/n_p}{R_s/n_p}\right)+\frac{R_p/n_p}{1+s(R_p/n_p)n_pC_d} = \frac{1}{n_p}\left[R_s\left(1+\frac{sL_s}{R_s}\right)+\frac{R_p}{1+sR_pC_d}\right] = \frac{1}{n_p}Z_{pv}. \quad (2.8)$$

Thus, for a generic n_s by n_p array:

$$Z_{pv}(s) = \frac{n_s}{n_p}Z_{pv\_mod}(s) \quad (2.9)$$

Under the assumptions of identical PV characteristics and circuit symmetry, series or parallel connections of the PV panels is reflected only as a dc shift in the PV impedance characteristics in frequency spectrum, without impacting the pole and zero locations. Thus, the dynamic characteristics of the PV do not change with series–parallel connections of multiple modules. The dynamic parameters are listed in Table 2. For this case study: $n_s = 11,\ n_p = 149$.

The Bode diagram of $Z_{pv}(s)$ is shown in Figure 2.4. $Z_{pv}(s)$ is characterized by a first order pole ω_p and a second order zero ω_z at approximately 10^4 rad/s and $9{\cdot}10^4$ rad/s, respectively. For angular frequencies lower than ω_p, the behavior of Z_{pv} can be approximated to that of a resistance:

$$|Z_{pv}(j\omega)| \cong |R_{pv}|, \qquad for\ \ \omega < \omega_p \quad (2.10)$$

Thus, at low frequencies the dynamic model can be simplified to a linear static model which is presented in the next section.

Table 2 – Dynamic parameters of the PV source

Dynamic Parameters of the PV Panel	Single module	Full Array
Dynamic resistance of the diode, r_d	4.5 Ω	0.33 Ω
Diffusion capacitance of the diode, C_d	22.2 µF	301 µF
Shunt resistance, R_{sh}	270 Ω	20 Ω
Total series resistance, R_s	370 mΩ	27 mΩ
Total series inductance, L_s	5.7 µH	0.42 µH
First order pole, ω_p	10^4 rad/s	
Second order zero, ω_z	$9\cdot10^4$ rad/s	

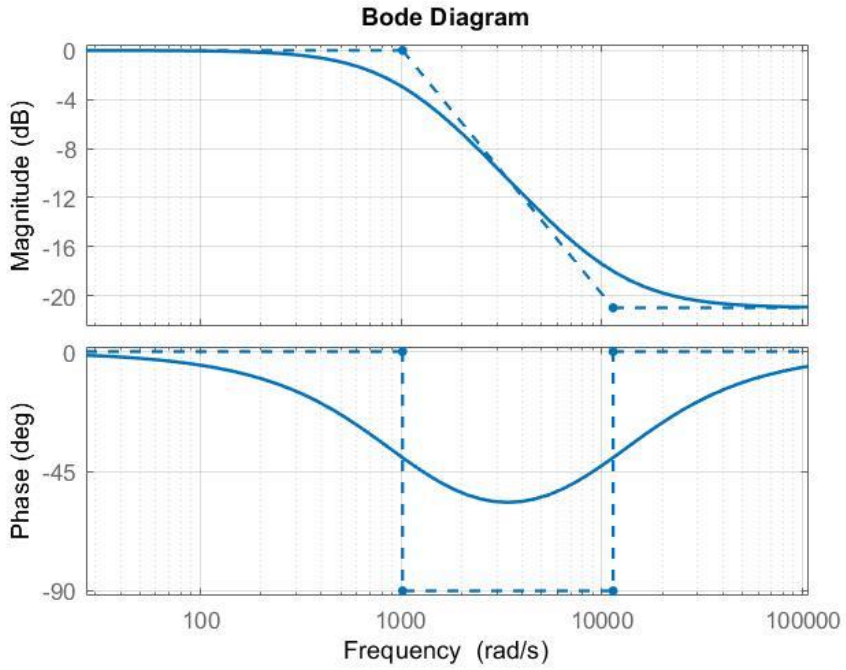

Figure 2.4 – Bode diagram of $Z_{pv}(s)$

2.2.2 Static Linear Model

The static linear model of the PV source is obtained by applying the Thevenin equivalent around the MPP on the I-V characteristic. Figure 2.5 shows a graphical representation of the linearization, highlighting the equivalent parameters.

The equivalent resistance R_{pv_eq} can be calculated by computing the differential of the I-V curve [10]:

$$\frac{\partial i_{pv}}{\partial v_{pv}} = -\frac{1}{R_{pv\_eq}} \tag{2.11}$$

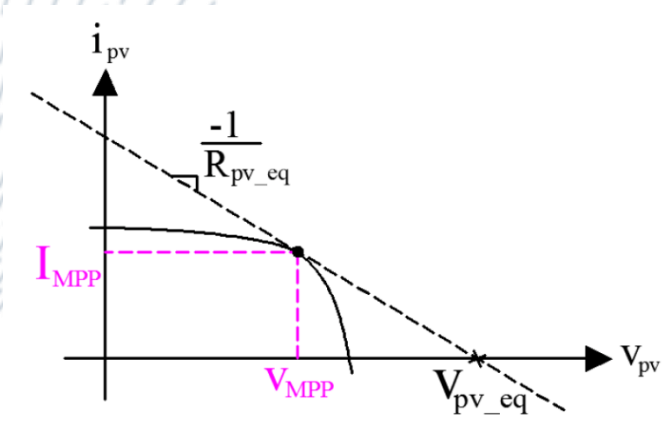

Figure 2.5 – Linearization around the MPP [3].

Table 3 – Static PV model parameters

Parameter	Value
R_{pv_eq}	1.56 Ω
V_{pv_eq}	852 V

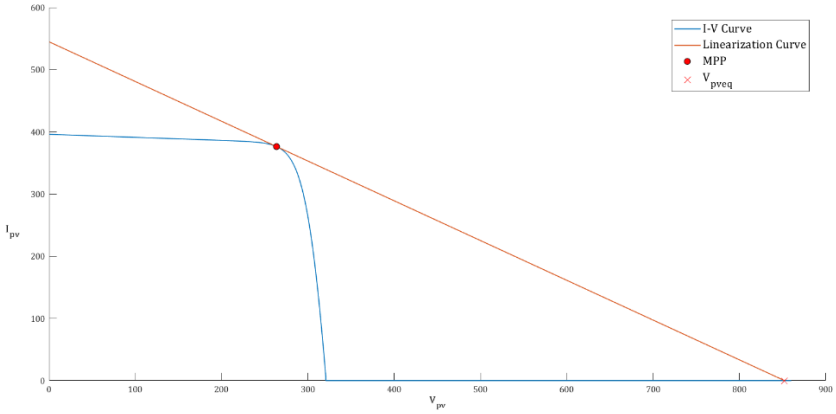

Figure 2.6 – Linearization of the I-V curve around the MPP (MatLab)

$$R_{pv\_eq} = \left(\frac{I_s + I_d}{\eta n_c V_t}\right)^{-1} + R_s \tag{2.12}$$

Where η indicated the diode's quality factor.

For this study however, the values of R_{pv_eq} and V_{pv_eq} have been extrapolated numerically from the I-V curve of the panel considered (Figure 2.6) and the values obtained are reported in Table 3.

2.3 Power Converters Model

In this section the small signal model of the system will be developed. The circuit in Figure 2.7 shows the double stage configuration with the static linear model of the PV source, the DC/DC boost converter and the DC/AC inverter connected to the external grid.

The electric circuit contains nonlinear components such as the switch and the diode of the DC/DC boost converter. The average operator is used to linearize the differential equations of the system: the switch operates at switching frequency $f_{sw} = 1/T_{sw} = 10\ kHz$, therefore any given variable $x(t)$ can be split into two states (on-state and off-state of the switch):

$$\frac{1}{T_{sw}}\int_0^{T_{sw}} x(t)dt = \frac{1}{T_{sw}}\left[\int_0^{dT_{sw}} x(t)dt + \int_{dT_{sw}}^{T_{sw}} x(t)dt\right] = d\bar{x}_{on} + (1-d)\bar{x}_{off} \tag{2.13}$$

Where $d = T_{on}/T_{sw}$ is the duty-cycle of the switch and $\bar{x}_{on}$, $\bar{x}_{off}$ are the average values of $x(t)$ during the on-state and off-state, respectively.

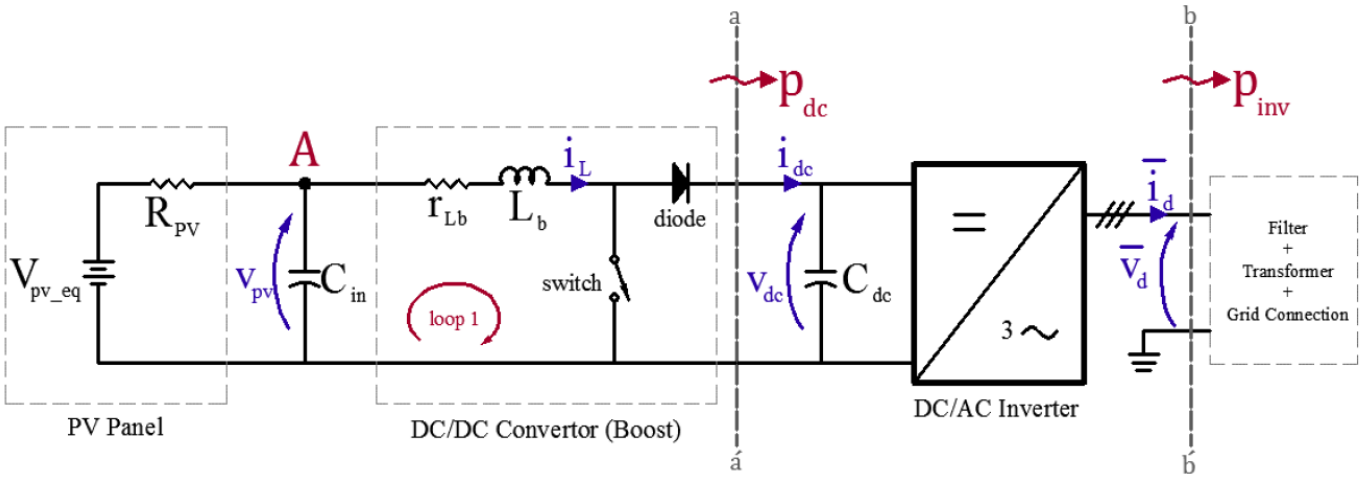

Figure 2.7 – Electric circuit of the power system [3].

The scheme of Figure 2.7 is used to write – for the two states of the system – the Kirchhoff's Current Law (KCL) at node A, the Kirchhoff's Voltage Law (KVL) at loop 1, and the power balance between sections *aa'* and *bb'*:

- On-state: $0 \leq t < dT_{sw}$

KCL: $$i_L(t) + C_{in}\frac{dv_{pv}(t)}{dt} + \frac{v_{pv}(t) - v_{pv\_eq}(t)}{R_{pv}} = 0 \quad (2.14)$$

KVL: $$-v_{pv}(t) + r_L i_L(t) + L_b\frac{di_L(t)}{dt} = 0 \quad (2.15)$$

aa'-bb': $$0 = p_{C\_dc}(t) + p_{inv}(t) \quad (2.16)$$

- Off-state: $dT_{sw} \leq t < T_{sw}$

KCL: $$i_L(t) + C_{in}\frac{dv_{pv}(t)}{dt} + \frac{v_{pv}(t) - v_{pv\_eq}(t)}{R_{pv}} = 0 \quad (2.17)$$

KVL: $$-v_{pv}(t) + r_L i_L(t) + L_b\frac{di_L(t)}{dt} + v_{dc}(t) = 0 \quad (2.18)$$

aa'-bb' $$p_{dc}(t) = p_{C\_dc}(t) + p_{inv}(t) \quad (2.19)$$

Bringing the derivative terms to the left-hand side of the KCL and KVL and expanding the terms in the power balance, the two sets of equations can be written as follows:

- On-state: $0 \leq t < dT_{sw}$

$$\frac{dv_{pv}(t)}{dt} = -\frac{1}{C_{in}}i_L(t) - \frac{1}{R_{pv}C_{in}}v_{pv}(t) + \frac{1}{R_{pv}C_{in}}v_{pv\_eq}(t) \quad (2.20)$$

$$\frac{di_L(t)}{dt} = -\frac{r_L}{L_b} i_L(t) + \frac{1}{L_b} v_{pv}(t) \tag{2.21}$$

$$0 = v_{dc}(t) \cdot C_{dc} \frac{dv_{dc}(t)}{dt} + v_d(t) \cdot i_d(t) \tag{2.22}$$

Where in equation (2.22) the quadrature component $v_q(t) \cdot i_q(t)$ of the power p_{inv} delivered to the grid has been neglected: assuming a small voltage drop on the filter, the magnitude of the Park voltage $\bar{v}_0$ is close to $\bar{v}$: $|V_0| = |V| \cong V_d$ and $v_{oq} = v_q = 0$.

- Off-state: $dT_{sw} \leq t < T_{sw}$

$$\frac{dv_{pv}(t)}{dt} = -\frac{1}{C_{in}} i_L(t) - \frac{1}{R_{pv} C_{in}} v_{pv}(t) + \frac{1}{R_{pv} C_{in}} v_{pv\_eq}(t) \tag{2.23}$$

$$\frac{di_L(t)}{dt} = -\frac{r_L}{L_b} i_L(t) + \frac{1}{L_b} v_{pv}(t) - \frac{1}{L_b} v_{dc}(t) \tag{2.24}$$

$$v_{dc}(t) \cdot i_{dc}(t) = v_{dc}(t) \cdot C_{dc} \frac{dv_{dc}(t)}{dt} + v_d(t) \cdot i_d(t) \tag{2.25}$$

The average operator is now applied to the equations with the assumption that the system operates under continuous conduction mode (CCM). Considering that $\bar{\imath}_{dc}(t) = (1-d) \cdot \bar{\imath}_L(t)$ the set of equations in the Laplace domain is:

$$s\bar{v}_{pv} = -\frac{1}{C_{in}} \bar{\imath}_L - \frac{1}{R_{pv} C_{in}} \bar{v}_{pv} + \frac{1}{R_{pv} C_{in}} \bar{v}_{pv\_eq} \tag{2.26}$$

$$s\bar{\imath}_L = -\frac{r_L}{L_b} \bar{\imath}_L + \frac{1}{L_b} \bar{v}_{pv} - \frac{1}{L_b} (1-d) \bar{v}_{dc} \tag{2.27}$$

$$\bar{v}_{dc} \cdot \bar{\imath}_L (1-d) = C_{dc} \bar{v}_{dc} \cdot s\bar{v}_{dc} + \bar{v}_d \cdot \bar{\imath}_d \tag{2.28}$$

The per-unit values are introduced considering as base values the rated apparent power A_b and the rated DC-bus voltage V_{dc_b}:

AC side
$$\begin{cases} V_{ac_b} = V_{dc_b}/\sqrt{2} \\ I_{ac_b} = A_b / V_{ac_b} \\ Z_{ac_b} = V_{ac_b} / I_{ac_b} \\ \omega_{ac_b} = \omega_n \end{cases} \tag{2.29}$$

DC side
$$\begin{cases} I_{dc_b} = A_b / V_{dc_b} \\ Z_{dc_b} = V_{dc_b} / I_{dc_b} \\ L_{dc_b} = Z_{dc_b} / \omega_{dc_b} \\ C_{dc_b} = 1/(\omega_{dc_b} Z_{dc_b}) \\ \omega_{dc_b} = 1\, rad/s \end{cases} \quad (2.30)$$

Equation (2.26) to (2.28) have been converted in per-unit (from now on, the average symbol is omitted to simplify the notation).

$$\dot{C}_{in} \frac{s}{\omega_{dc_b}} \dot{v}_{pv} = -i_L - \frac{1}{\dot{R}_{pv}} \dot{v}_{pv} + \frac{1}{\dot{R}_{pv}} \dot{v}_{pv\_eq} \quad (2.31)$$

$$\dot{L}_b \frac{s}{\omega_{dc_b}} i_L = -\dot{r}_L i_L + \dot{v}_{pv} - (1-d)\dot{v}_{dc} \quad (2.32)$$

$$\dot{v}_{dc} \cdot i_L (1-d) = \dot{C}_{dc} \dot{v}_{dc} \cdot \frac{s}{\omega_{dc_b}} \dot{v}_{dc} + \dot{v}_d \cdot i_d \quad (2.33)$$

The small variation approach is now introduced for all the variables except for $v_{pv\_eq} = V_{pv\_eq}$ and $v_d = V_d$ that are considered constant:

$$\begin{cases} v_{pv} = V_{pv} + \Delta v_{pv} \\ v_{dc} = V_{dc} + \Delta v_{dc} \\ d = D + \Delta d \end{cases} \qquad \begin{cases} i_L = I_L + \Delta i_L \\ i_{dc} = I_{dc} + \Delta i_{dc} \\ i_d = I_d + \Delta i_d \end{cases} \quad (2.34)$$

Equations (2.31) to (2.33) can now be split into two sets of steady state and small signal equations respectively:

- Steady state equations:

$$-I_L - \frac{V_{pv}}{R_{pv}} + \frac{V_{pv\_eq}}{R_{pv}} = 0 \quad (2.35)$$

$$-r_L I_L + V_{pv} - (1-D)V_{dc} = 0 \quad (2.36)$$

$$V_{dc} I_L (1-d) - V_d I_d = 0 \quad (2.37)$$

- Small signal equations:

$$C_{in} \frac{s}{\omega_{dc_b}} \Delta v_{pv} = -\Delta i_L - \frac{1}{R_{pv}} \Delta v_{pv} \quad (2.38)$$

$$L_b \frac{s}{\omega_{dc_b}} \Delta i_L = -r_L \Delta i_L + \Delta v_{pv} - \Delta v_{dc} + D\Delta v_{dc} + \Delta d V_{dc} + \Delta d \Delta v_{dc} \quad (2.39)$$

$$-V_{dc}I_L\Delta d + V_{dc}\Delta i_L(1-D) - V_{dc}\Delta i_L\Delta d + I_L\Delta v_{dc}(1-D) - I_L\Delta v_{dc}\Delta d + (1-D)\Delta v_{dc}\Delta d - v_{dc}\Delta d^2 = C_{dc}V_{dc}\frac{s\Delta v_{dc}}{\omega_{dc_b}} + C_{dc}\Delta v_{dc}\frac{s\Delta v_{dc}}{\omega_{dc_b}} + V_d\Delta i_d \quad (2.40)$$

Finally, by neglecting second order terms ($\Delta d\Delta v_{dc} \approx \Delta i_L\Delta d \approx \Delta v_{dc}\Delta v_{dc} \approx 0$) and by rearranging the variables, gives:

$$\left(s + \frac{\omega_{dc_b}}{R_{pv}C_{in}}\right)\Delta v_{pv} = -\frac{\omega_{dc_b}}{C_{in}}\Delta i_L \quad (2.41)$$

$$\left(s + \frac{\omega_{dc_b}r_L}{L_b}\right)\Delta i_L = \frac{\omega_{dc_b}}{L_b}\Delta v_{pv} - \frac{\omega_{dc_b}(1-D)}{L_b}\Delta v_{dc} + V_{dc}\frac{\omega_{dc_b}}{L_b}\Delta d \quad (2.42)$$

$$\left[I_L(1-D) - \frac{s\,C_{dc}V_{dc}}{\omega_{dc_b}}\right]\Delta v_{dc} = V_{dc}I_L\Delta d - V_{dc}(1-D)\Delta i_L + V_d\Delta i_d \quad (2.43)$$

Equations (2.41) to (2.43) describe the small signal model of the power converters and the PV source linearized around the working point (MPP). These equations will be used in section 2.5 to deduce the transfer function of the full system.

2.4 Current-Controlled Synthetic Inertia Control

Reference [11] and [5] studied a system model consisting of a three-phase converter interfaced to an external grid by means of an LC filter and a transformer (Figure 2.8). The external grid is represented by an inductive-resistive impedance in series with a sinusoidal voltage source.

The regulation performed by the grid-supporting units can be analyzed starting from the circuit of Figure 2.8. Neglecting parasitic losses, the instantaneous power balance of the network is:

$$p_g + p_{out} + p_{conv} = 0 \quad (2.44)$$

Where:

- p_g represents the load absorption;
- p_{out} is the instantaneous contribution from the grid-supporting units;
- p_{conv} is the power injected by the grid-following converter.

Referring to the differential model, the power balance becomes:

$$\Delta p_g + \Delta p_{out} + \Delta p_{conv} = 0 \quad (2.45)$$

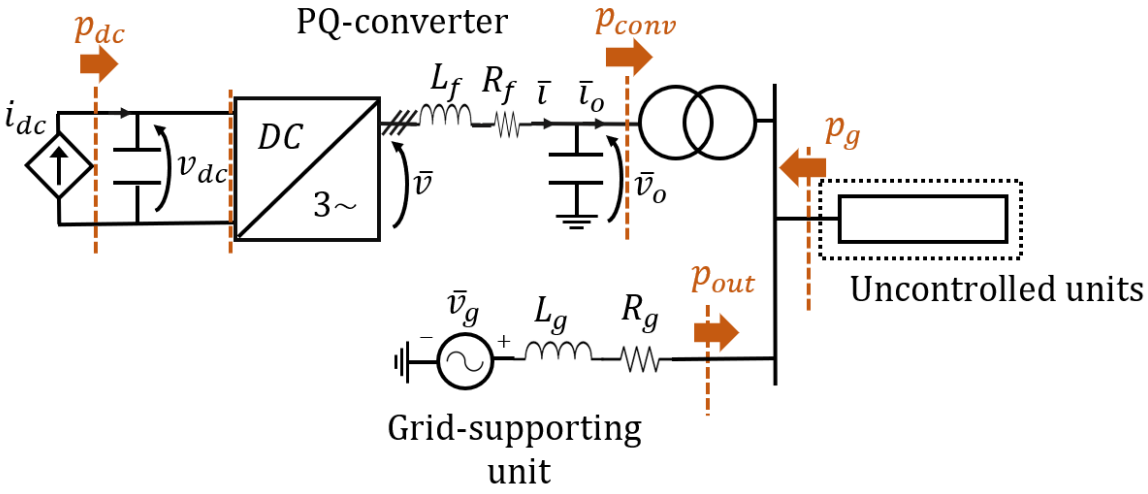

Figure 2.8 – Structure of the system with conventions adopted for power measurements [5]

Where:

- Δp_g is the variation of load absorption ($\Delta p_g < 0$ for active load increase, $\Delta p_g > 0$ for active load decrease);
- Δp_{out} is the contribution from physical inertias in the system and from primary regulation;
- Δp_{conv} is the contribution from the PQ-converter.

Assuming that no synthetic inertia is provided from the PQ-converter ($\Delta p_{conv} = 0$), a change of the local load $\Delta p_g \neq 0$ causes the system angular frequency ω to undergo a transient. Moreover, the GSU output power variation Δp_{out} changes according to two effects:

- The kinetic energy variation from physical inertias in the system;
- The stabilizing effect provided by the primary frequency regulation.

$$\Delta p_{out} = \Delta p_{inertia} + \Delta p_{reg} \tag{2.46}$$

➢ As regards primary regulation, according to national directives the active power injection must compensate frequency transients according to a negative proportional law with a droop coefficient $m = \frac{1}{K_{reg}} = 2{,}4\%$ (Figure 2.9).

When the frequency variation $\Delta\omega$ occurs, the power modulation Δp_{reg} happens after a time delay τ associated to the internal dynamics of the plant. Thus, the primary regulation effect can be expressed (2.47) by (2.48) and for time and Laplace domains respectively:

$$\Delta p_{reg} = -K_{reg} \cdot \Delta\omega(t - \tau) \tag{2.47}$$

$$\Delta p_{reg} = -K_{reg} \cdot \Delta\omega \cdot e^{-s\tau} \cong -K_{reg} \frac{1}{1 + s\tau} \cdot \Delta\omega \tag{2.48}$$

Where the regulating energy is:

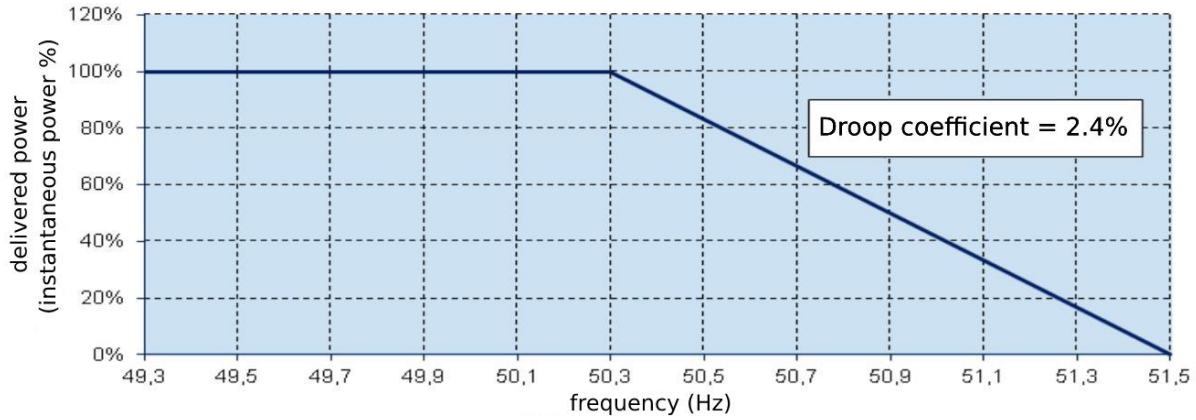

Figure 2.9 – Regulation of active power injection as a function of the frequency [12].

$$K_{reg} = -\frac{\Delta p_{reg}}{\Delta\omega} = -\frac{0 - 1\ p.u.}{\frac{51{,}5 - 50{,}3\ Hz}{50\ Hz}} = \frac{1}{2{,}4\%} \cong 41{,}7\ p.u. \tag{2.49}$$

- Regarding the effects of physical inertias, they can be considered referring to the swing equation which models the linearized behavior associated to the kinetic energy derivative: an angular frequency change $\Delta\omega$ on the external system produces a variation of the injected power $\Delta p_{inertia}$ according to:

$$\Delta p_{inertia} \cdot A_b = -\Delta p \left[\frac{1}{2} J \left(\frac{\omega_g \omega_b}{n}\right)^2\right] = -\frac{J {\omega_b}^2}{n^2} \omega^0 p \Delta\omega \tag{2.50}$$

Where:

- $p = \frac{d}{dt}$
- J is the total moment of inertia associated to the system.
- ω is the per-unit angular frequency in electrical degrees.
- n is the number of pole-pairs of the equivalent machine.

And it was assumed that before the transient occurrence, the system was operating under normal conditions ($\omega^0 \cong 1\ pu$).

The negative sign comes from the convention of measuring the delivered power as positive. Defining the equivalent starting time as $T_a \triangleq J{\omega_b}^2/n^2 A_b$, equation (2.50) becomes, in the Laplace domain:

$$\Delta p_{inertia} = -T_a \cdot s\Delta\omega \tag{2.51}$$

The inertia contribution $\Delta p_{inertia}$ is positive when $\Delta\omega < 0$, that is the machine injects power into the grid when the angular frequency reduces, as the kinetic energy of the rotating masses decreases.

Substituting (2.48) and (2.51) in (2.46) leads to the dynamical model of Figure 2.10 and expressed by the following equation (assuming no synthetic inertia, $\Delta p_{conv} = 0$):

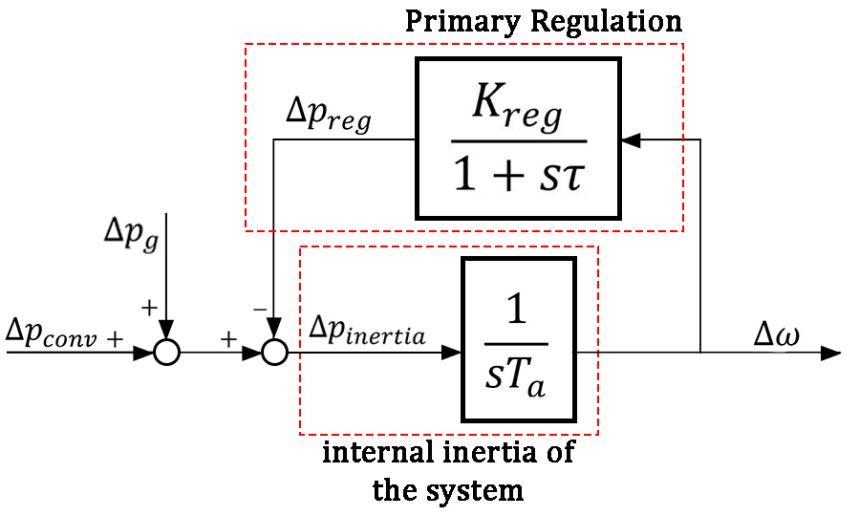

Figure 2.10 – Dynamic linear model of the grid used for frequency transients' analysis.

$$\Delta p_{out} = \Delta p_{inertia} + \Delta p_{reg} = \left(-sT_a - \frac{K_{reg}}{1+s\tau}\right) \cdot \Delta\omega \tag{2.52}$$

$$\Delta\omega = -\frac{1+s\tau}{s^2 T_a \tau + sT_a + K_{reg}} \cdot \Delta p_{out} \tag{2.53}$$

And as $\Delta p_g + \Delta p_{out} + \Delta p_{conv} = 0$, with $\Delta p_{conv} = 0$ it results:

$$\Delta\omega = \frac{1+s\tau}{s^2 T_a \tau + sT_a + K_{reg}} \cdot \Delta p_g \tag{2.54}$$

In case the nominal power is different from the base one, the grid parameters T_a and K_{reg} shall be modified following the typical equivalences: $T_a' = T_a \cdot \frac{A_{n1}}{A_b}$ and $K'_{reg} = K_{reg} \cdot \frac{A_{n1}}{A_b}$.

The fundamental frequency of the grid considers the primary regulation performed by the supporting unit and the equivalent inertia of the system. Typically, the PQ converter acts as a constant power source, thus $\Delta p_{conv} = 0$. Under these conditions the primary frequency regulation can be modelled according to (2.55) and (2.56):

$$\omega_g = \omega_{gn} + K_g(s) \cdot \Delta p_g \tag{2.55}$$

$$K_g(s) = \frac{\Delta\omega_g}{\Delta p_g} = \frac{(1+s\tau)}{s^2 T_a \tau + sT_a + K_{reg}} = \frac{(1+s\tau)}{s^2 \frac{1}{{\omega_n}^2} + s\frac{2\xi}{\omega_n} + 1} \tag{2.56}$$

where $K_g(s)$ is the equivalent transfer function of the grid, which is characterized by two complex conjugate poles with natural frequency ω_n and damping factor ξ:

$$\omega_n = \sqrt{\frac{K_{reg}}{T_a \tau}} \tag{2.57}$$

$$\xi = \frac{1}{2}\sqrt{\frac{T_a}{\tau K_{reg}}} \tag{2.58}$$

In the case that $\xi < \sqrt{2}/2$ (that is $\tau > T_a/2K_{reg}$), the Bode diagram shows a resonance peak in correspondence to the grid natural frequency $\omega_n \cong 126\ rad/s$. Figure 2.11 shows the Bode diagrams for the transfer function of the GSU.

Figure 2.12 shows the general structure of the control system: as in a traditional PQ scheme, an external DC-bus control with a slow pass-band defines the reference for the internal active power control; as for the reactive contribution it is assumed an external constant reference Q_{ref}. A frequency-locked loop (FLL) estimates the derivative of the angular frequency $\widetilde{\omega}_g$; the inertia control behaves as an additional active power reference proportional to the frequency approximate derivative $\widetilde{\omega}_g$. An independent phase-locked loop (PLL) determines the estimated synchronous control frame $\tilde{d}\tilde{q}_s$.

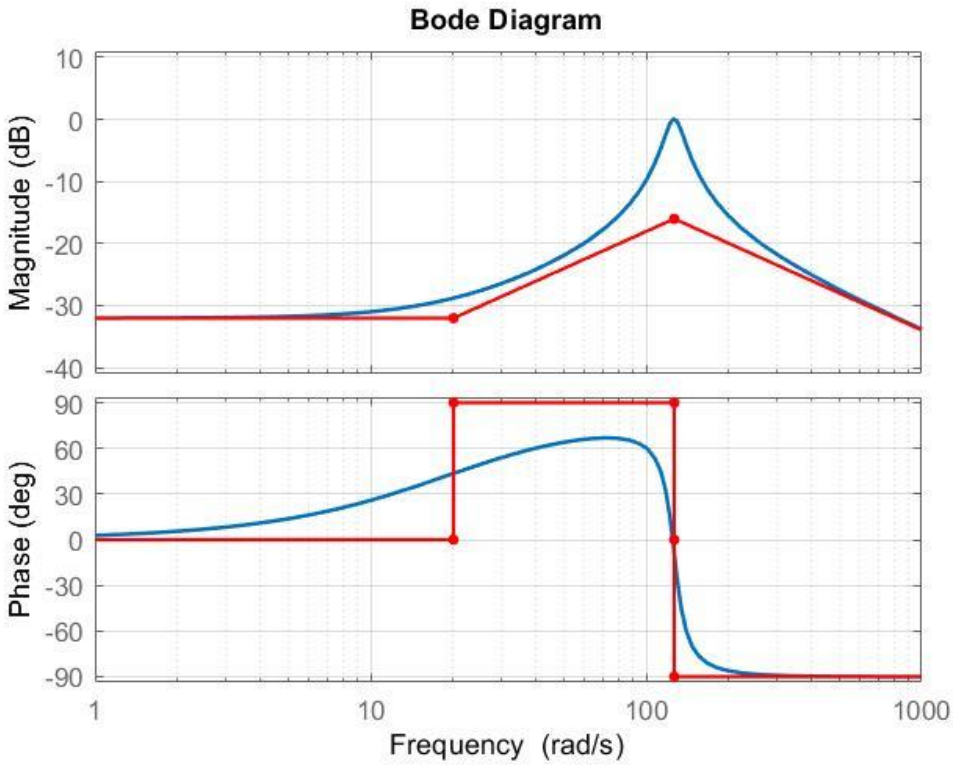

Figure 2.11 – Bode diagram for $K_g(s)$

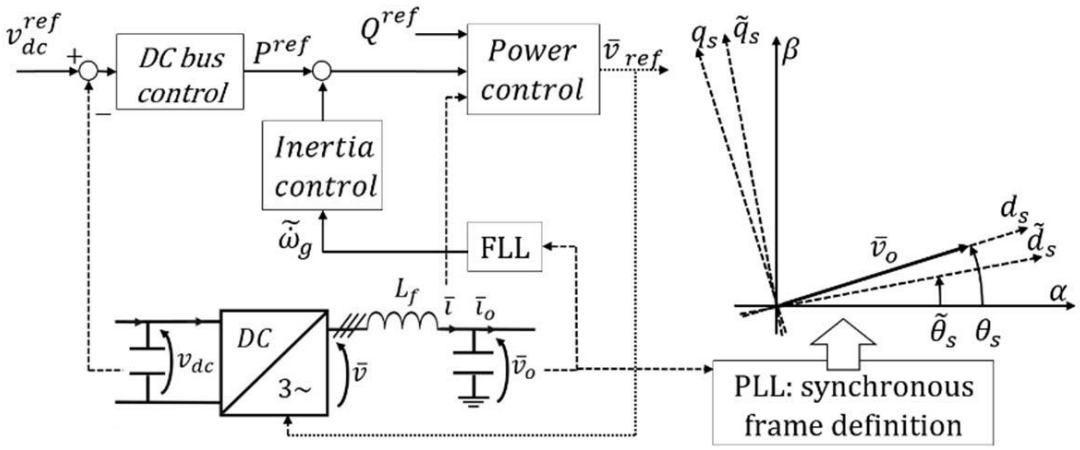

Figure 2.12 – Structure of the converter [11].

A second-order generalized integrator (SOGI) algorithm [5] has been introduced to separate the derivative estimation (FLL) from the synchronous frame definition (PLL) to increase the degrees of freedom associated to the design of the control system.

The linear model developed in [11] is reported in Figure 2.13 in which the following assumptions have been made:

- The effect associated to the PLL is negligible: $\theta_s - \tilde{\theta}_s \cong 0$; a single dq frame with angular frequency ω_s is considered.
- Assuming a small voltage drop on the filter, the magnitude of the Park voltage $\bar{v}_0$ is close to $\bar{v}$: $|V_0| = |V| \cong V_d$ and $v_{oq} = v_q = 0$.
- Low losses are assumed on the filter: $p_{inv} = Re\{\bar{v}_{dq\_s}\bar{\imath}^*_{dq\_s}\} \cong p_{conv} = Re\{\bar{v}_{o\ dq\_s}\bar{\imath}^*_{o\ dq\_s}\}$.

The design of the selective inertia is performed including the external grid model into the linearized system. This model allows to derive the equivalent open-loop function associated to the inertia control (Figure 2.14), which is given by:

$$L(s) = \frac{s}{1 + s/\omega_{FLL}} \cdot \frac{K_{in}}{1 + s\tau_{in}} \cdot K_g(s) \cdot KI(s) \tag{2.59}$$

Neglecting the effect of the internal current control which is generally much faster than the considered dynamics ($KI(s) \cong 1$), the open loop function associated to the inertia control becomes:

$$L(s) \cong \frac{s}{1 + s/\omega_{FLL}} \cdot \frac{K_{in}}{1 + s\tau_{in}} \cdot \frac{(1 + s\tau)}{s^2 T_a \tau + sT_a + K_{reg}} \tag{2.60}$$

which, for $\omega < 1/\tau_{in}$, gives an approximate closed loop function:

$$K'_g(s) = \frac{\Delta\omega_g}{\Delta p_g} = \frac{K_g(s)}{1 + L(s)} \cong \frac{(1 + s\tau)}{s^2(T_a\tau + K_{in}\tau) + s(T_a + K_{in}) + K_{reg}} \tag{2.61}$$

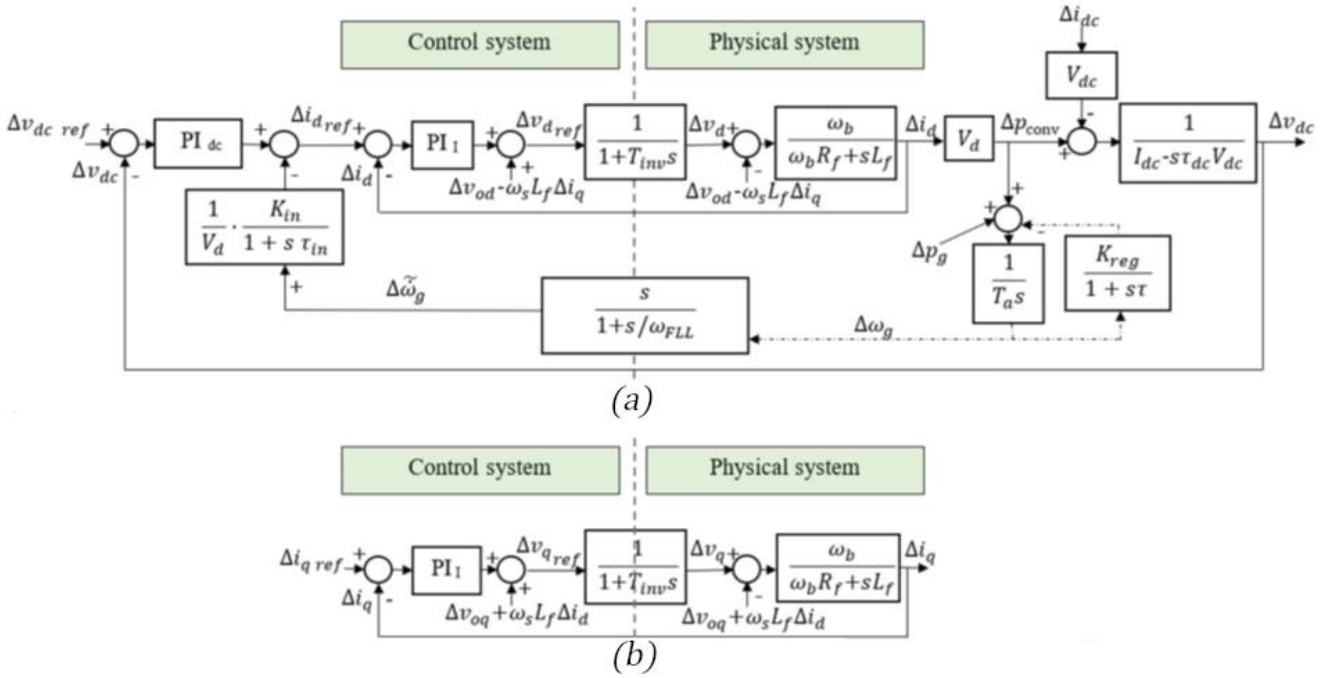

Figure 2.13 – Linearized model for the design of the control system: direct (a) and quadrature (b) axis [11].

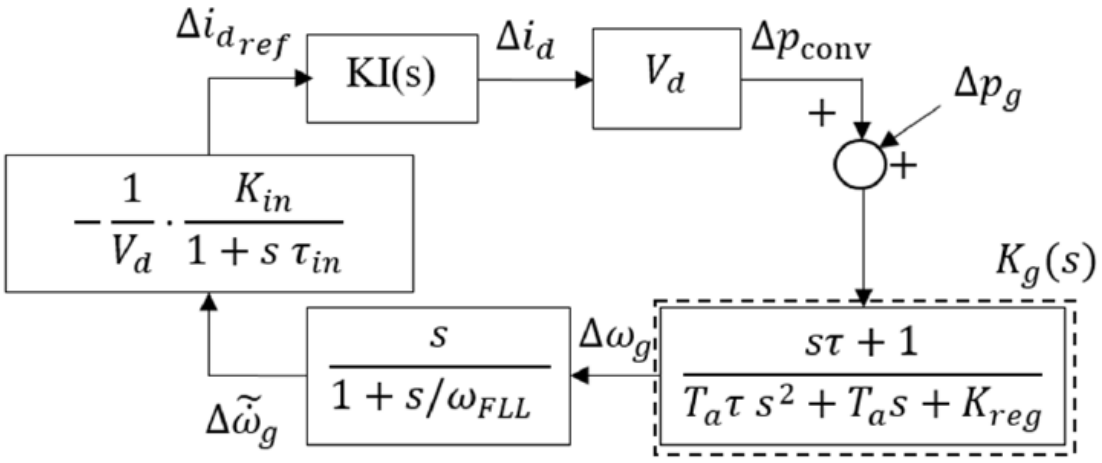

Figure 2.14 – Equivalent control loop associated to the inertia regulation [11].

The introduction of the synthetic inertia provision moves the poles of the grid to lower frequencies $\omega'_n = \sqrt{K_{reg}/(T_a\tau + K_{in}\tau)}$ and increases the damping factor $\xi = 0.5\sqrt{(T_a + K_{in})/\tau K_{reg}}$ contributing to the slow-down of the corresponding transient and increasing their equivalent damping; the magnitude of the resonance peak reduces according to the diagram shown in Figure 2.15. A sufficient condition for stability is $L(j\omega_p) < 1$, thus:

$$\frac{K_{in}}{T_a} < \sqrt{\frac{T_a}{\tau K_{reg}}} \tag{2.62}$$

2.5 Transfer Function Diagram

In this section the complete transfer function block diagram will be extracted starting from the small signal equations found previously. Rearranging equation (2.41) and (2.43) respectively gives:

$$\Delta i_L = -\frac{C_{in}}{\omega_{dc_b}}\left(s + \frac{\omega_{dc_b}}{R_{pv}C_{in}}\right)\Delta v_{pv} \tag{2.63}$$

$$\Delta v_{dc} = \frac{V_{dc}I_L\Delta d - V_{dc}(1-D)\Delta i_L + V_d\Delta i_d}{I_L(1-D) - \frac{s\,C_{dc}V_{dc}}{\omega_{dc_b}}} \tag{2.64}$$

Substituting (2.63) into (2.64) gives Δv_{dc} as a function of Δd, Δv_{pv} and Δi_d:

$$\Delta v_{dc} = \frac{V_{dc}I_L\Delta d + V_{dc}(1-D)\frac{\omega_{dc_b}}{C_{in}}\left(s + \frac{\omega_{dc_b}}{R_{pv}C_{in}}\right)\Delta v_{pv} + V_d\Delta i_d}{I_L(1-D) - \frac{s\,C_{dc}V_{dc}}{\omega_{dc_b}}} \tag{2.65}$$

Δv_{pv} is obtained by combining equation (2.41) and (2.42):

$$\Delta v_{pv} = \frac{\frac{{\omega_{dc_b}}^2(1-D)}{L_bC_{in}}\Delta v_{dc} - \frac{{\omega_{dc_b}}^2V_{dc}}{L_bC_{in}}\Delta d}{M_1(s)} \tag{2.66}$$

Where the denominator $M_1(s)$ is equal to:

$$M_1(s) = s^2 + \omega_{dc_b}\left(\frac{r_L}{L_b} + \frac{1}{R_{pv}C_{in}}\right)s + \frac{{\omega_{dc_b}}^2}{L_bC_{in}}\left(\frac{r_L}{R_{pv}} + 1\right) \tag{2.67}$$

Equations (2.63), (2.65) and (2.66) give the concept of physical system with its correlations which in addition to control regulators and loops make it possible to illustrate the overall system transfer function diagram as shown in Figure 2.16.

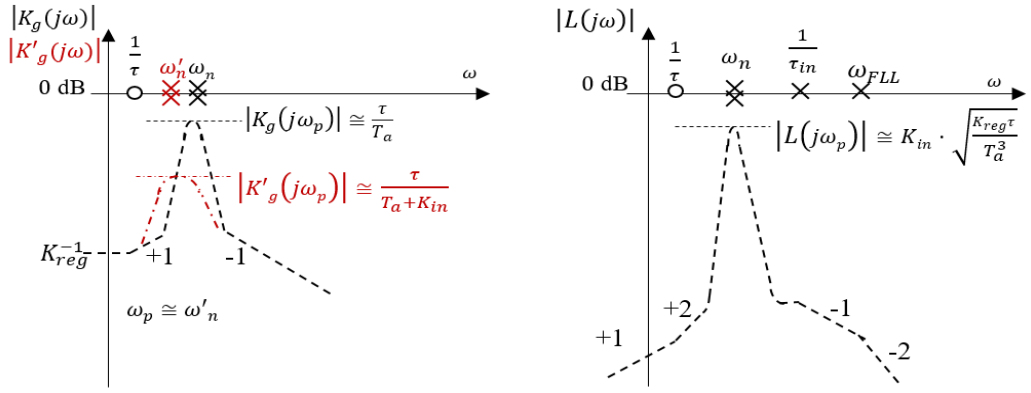

Figure 2.15 – (a) Equivalent grid function without synthetic inertia (black dashed line) and with synthetic inertia (red dashed-dotted line); (b) open-loop transfer function of the selective inertia loop [11].

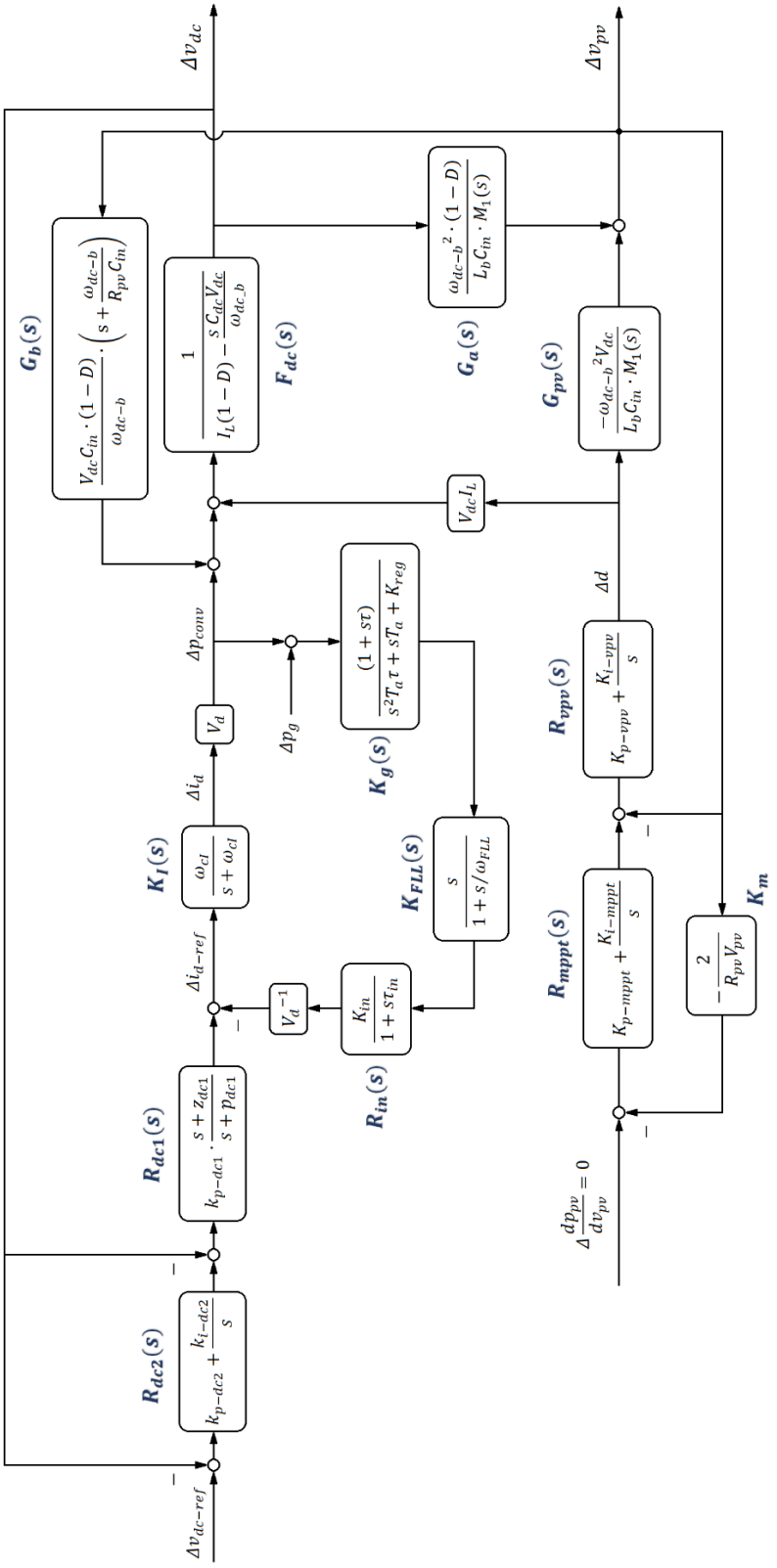

Figure 2.16 – Full system transfer function diagram

3. Chapter three

Physical Components and Controllers' Design

This chapter is dedicated to the sizing of the physical components of the system and to the design of the controllers' parameters. The first two sections deal with the design of the physical components, namely the LCL filter on the AC-side, the DC-Bus and PV-Bus capacitors and the DC-DC converter input inductance. Sections 0 to 3.5 deal with the tuning of the regulators for inertia provision, the DC-Bus voltage control and the MPPT and PV source voltage.

3.1 LCL Filter Design

The design choices used for sizing the AC-side passive filter are reported in this section. The structure of the LCL filter is reported in Figure 3.1.

- The parameters L_g and R_g represent the transformer and the external grid. Considering that the power delivered by the system is 500 kVA, it can be assumed that, for a transformer of this size, the short circuit voltage drop is equal to $v_{kn} = 4\%$. Moreover, the value of the resistance R_g is usually very small and can be neglected. Thus the transformer's reactance can be calculated as:

$$X_{Lg} = v_{kn} \cdot \frac{\left(\sqrt{3}\, V_{ph-n}\right)^2}{A_n} = 67.4\ m\Omega \tag{3.1}$$

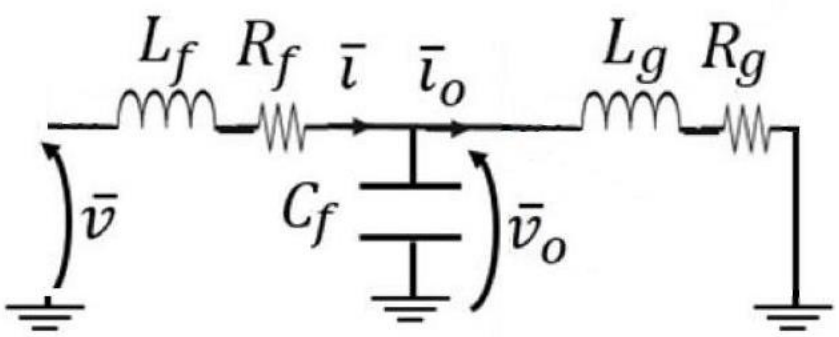

Figure 3.1 – Structure of the LCL filter

Which gives $L_g = 215\,\mu H$. Where $V_{ph-n} = 530\,V$ is the nominal phase voltage on the primary side and $A_n = 500\,kVA$ is the rated power of the transformer.

- The 3-phase capacitor C_f is designed assuming that its reactive power equals 5% of the power delivered by the inverter:

$$3\,\omega_n\,C_f\,{V_{ph-n}}^2 = 0.05\,A_n \tag{3.2}$$

Which gives $C_f = 94.5\,\mu F$. The resistance R_{Cf} is estimated as one third of the capacitor's impedance at switching frequency $f_{sw} = 4\,kHz$:

$$R_{Cf} = \frac{1/3}{2\pi f_{sw} C_f} = 140\,m\Omega \tag{3.3}$$

- The inductor L_f is sized in such a way that the total voltage drop considering L_g and R_g must be less than 5%:

$$(X_{Lf} + X_{Lg})I_n < 0.05\,V_n \tag{3.4}$$

Where $I_n = A_n/3V_{ph-n} = 314\,A$.

$$X_{Lf} < \frac{0.05\,V_n - X_{Lg}I_n}{I_n} = 168\,m\Omega \tag{3.5}$$

Assuming that the quality factor of the inductor is $Q = \omega_n L_f / R_{Lf} = 100$, it results:

$$L_f = \frac{X_{Lf}}{\omega_n} = 53.6\,\mu H \tag{3.6}$$

$$R_{Lf} = \frac{\omega_n L_f}{100} = 0.168\,m\Omega \tag{3.7}$$

The numerical values of the LCL filter are reported in Table 4.

Table 4 – LCL filter parameters

Parameter	Value	
L_f	53.6 µH	0.03 p.u.
R_{Lf}	0.168 mΩ	2.99e-4 p.u.
C_f	94.5 µF	0.0167 p.u.
R_{Cf}	0.14 Ω	0.249 p.u.
L_g	215 µH	0.120 p.u.

3.2 DC Components Design

This section presents the criteria used for the design of the following components:

- the DC-Bus capacitor C_{dc};
- the DC-DC converter input inductance L_b;
- the PV-Bus capacitor C_{in}.

The steady state values of the variables that have been used for the sizing are reported in Table 5.

- As regards the DC-Bus capacitor C_{dc}, its main purpose is to act as an energy buffer for inertia provision, able to supply 10% of the system's rated power A_b during frequency transients. When a drop in the grid frequency occurs, the control system lowers the DC-Bus voltage allowing C_{dc} to deliver power to the grid. The energy balance equation (3.9) allows to determine the lower bound for C_{dc}:

$$\frac{1}{2}C_{dc}({V_{dc}}^2 - {V_{dc\_min}}^2) \geq 0.1\ A_b \Delta t^* \tag{3.8}$$

$$C_{dc} \geq 2\frac{0.1\ A_b \cdot \Delta t^*}{({V_{dc}}^2 - {V_{dc\_min}}^2)} \cong 29.96\ mF \qquad \rightarrow C_{dc} = 30\ mF \tag{3.9}$$

  Where:
  - $V_{dc\_min} = 90\%\ V_{dc}$, is the minimum voltage of the DC-Bus.
  - $\Delta t^* = 4\tau_n$, is the presumed duration of the frequency transient with $\tau_n = 1/\omega_n$ being the time constant of the external grid;
  - $A_b = 500\ kVA$ is the system's rated power.

- For the sizing of the DC-DC converter input inductance L_b, the maximum current ripple criterion is used:

$$\Delta I_{pv} \leq \frac{V_{pv} D}{L_b f_{sw}} \tag{3.10}$$

  Where ΔI_{pv} is the PV-Bus current ripple whose maximum value is set to be equal to 1% of the nominal current: $\Delta I_{pv\_max} = 2.5\% \rightarrow I_{pv} = 20.8\ A$. From (3.10) the minimum value of L_b can be obtained:

$$L_b \geq \frac{V_{pv} D}{f_{sw}\ \Delta I_{pv\_max}} \cong 1.43\ mH \qquad \rightarrow L_b = 1.5\ mH/831A \tag{3.11}$$

  Where the final value $L_b = 1.5\ mH$ has been rounded up to keep some margin.

Table 5 – Steady state values of the system's variables

Steady State Variables	Symbol	Values
PV-Bus voltage and current	V_{pv}, I_{pv}	602 [V], 831 [A]
DC-Bus voltage and current	V_{dc}, I_{dc}	750 [V], 667 [A]
Switching frequency	f_{sw}	4 [kHz]
Duty cycle	D	0.197

- As regards the PV-Bus capacitor C_{in}, it is designed to make sure that the current ripple ΔI_{pv_max} flows mainly through the capacitor instead of the PV panel. The scheme of Figure 3.2 shows the equivalent circuit of the PV-Bus at switching frequency $f_{sw} = 4\ kHz$. The impedance of the PV panel has been calculated according to the dynamic model equations (2.4) and (2.9): $|Z_{pv}| \cong 0.127\ \Omega$, at $\omega = 2\pi f_{sw}$ and the DC-DC converter is modeled as an ideal current source of amplitude equal to the maximum current ripple ΔI_{pv_max}.
- The absolute value of the impedance of C_{in} is set to be at least an order of magnitude smaller than $|Z_{pv}|$:

$$\left|\frac{1}{j2\pi f_{sw} C_{in}}\right| \leq \frac{1}{10}|Z_{pv}| \tag{3.12}$$

- Which gives:

$$C_{in} \geq \frac{10}{2\pi f_{sw}|Z_{pv}|} \cong 3.14\ mF \qquad \rightarrow C_{in} = 5\ mF \tag{3.13}$$

- Where the final value $C_{in} = 5\ mF$ has been rounded up to keep some margin. Table 6 reports the final values of the components deigned in this section.

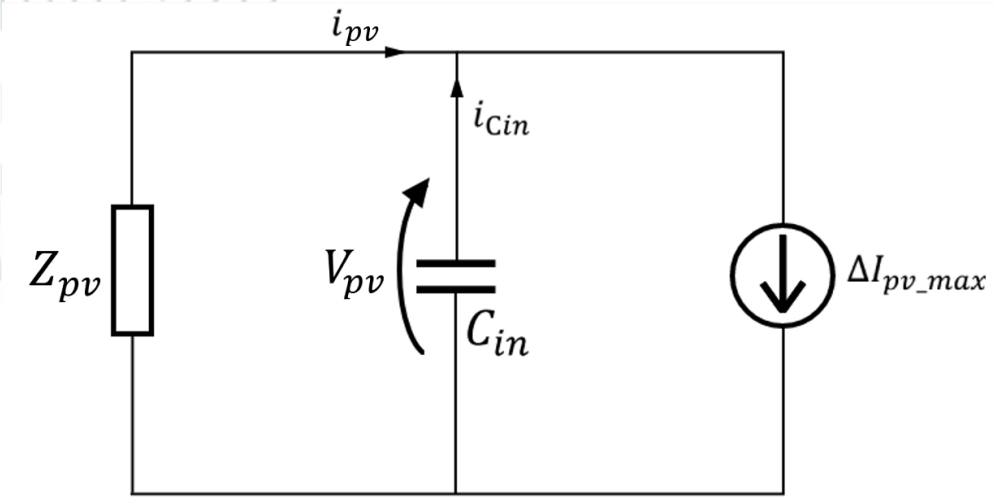

Figure 3.2 – Equivalent circuit for the PV-Bus capacitor sizing

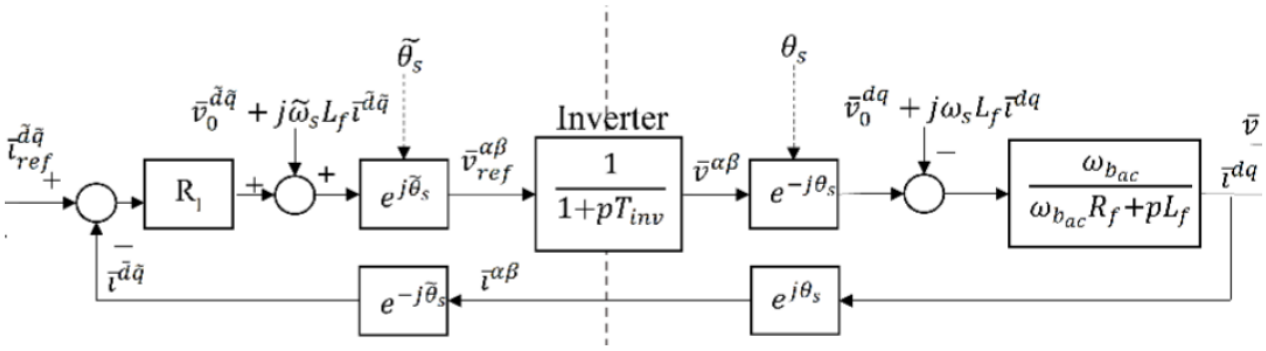

Figure 3.3 – Current control loop diagram for the DC/AC inverter [11].

Table 6 – DC-bus and PV-bus parameters

Parameter	Value	
C_{dc}	30 mF	33.8e-3 p.u.
L_b	1.5 mH	1.3e-3 p.u.
C_{in}	5 mF	5.6e-3 p.u.

3.3 Current Control Loop

The current loop for the DC/AC inverter is represented in Figure 3.3. Knowing that $T_{inv} \ll 1$, the transfer function of the inverter can be approximated equal to one. The equivalent load function $G_f(s)$ is given by:

$$G_f(s) = \frac{\omega_{b-ac}}{\omega_{b-ac} R_{Lf} + sL_f} \tag{3.14}$$

Where $\omega_{b-ac} = 2\pi \cdot 50\ rad/s$ is the AC-side base angular frequency.

The load function is characterized by a low frequency pole in $\omega_f = \omega_{b-ac} R_{Lf}/L_f \cong 3.13\ rad/s$. Therefore, the cut-off frequency of the open loop function $L_I(s) = R_I(s) \cdot G_f(s)$ is set to be $\omega_{cI} = 40\ rad/s$, where $R_I(s)$ is the PI regulator $R_I(s) = k_{pI} + k_{iI}/s$.

Figure 3.4 shows the Bode diagrams associated to the current control loop and

Table 7 reports the parameters of the regulator.

Table 7 - Parameters of the current PI regulator $R_I(s)$

Parameter	Value
Proportional coefficient, k_{p-I}	0.00348 p.u.
Integral coefficient, k_{i-I}	0.00635 p.u/s
Cut-off frequency of the open loop, ω_{cI}	40 rad/s

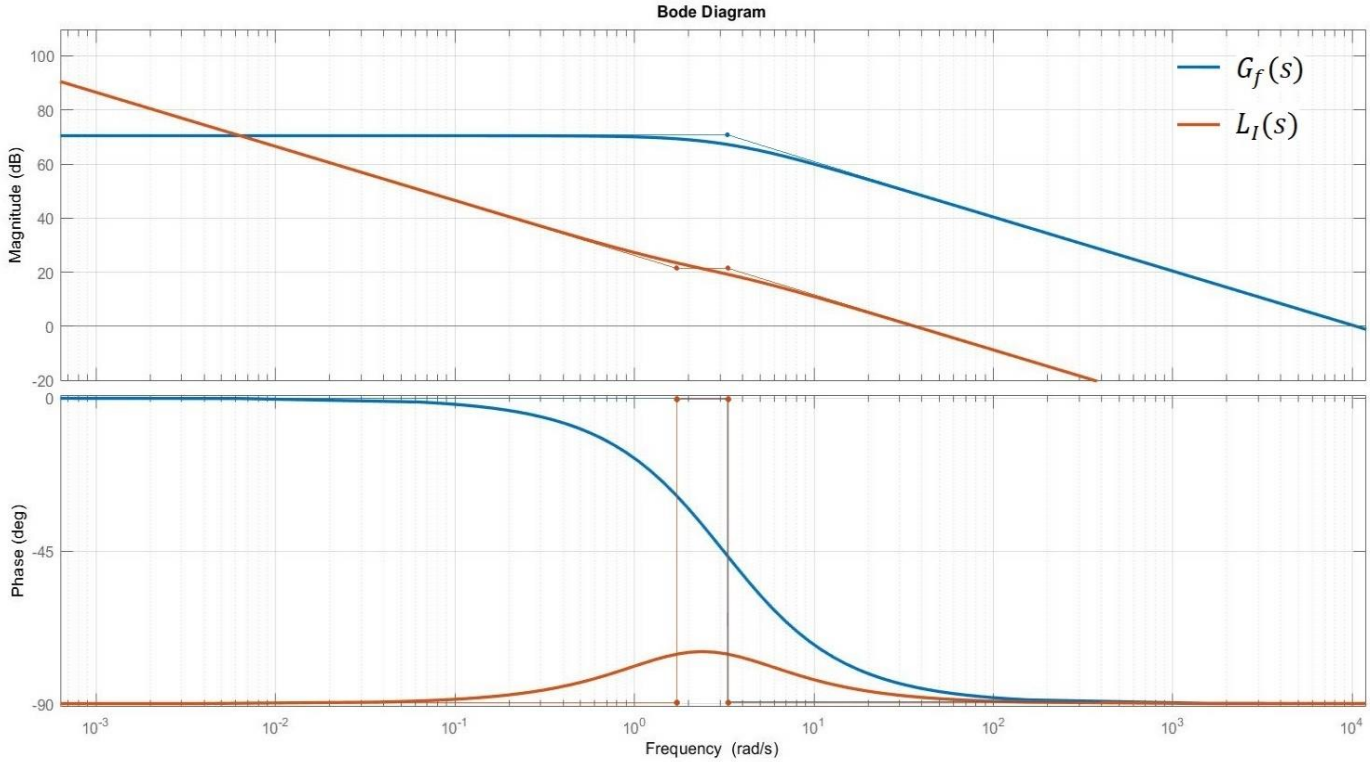

Figure 3.4 - Bode diagram of the current loop functions $G_f(s)$ and $L_I(s)$

3.4 DC-Bus Voltage Control Loop

The DC-Bus control loop is going to be designed with a desired cut off frequency equal to $\omega_{c-vdc} = 1\,rad/s$. The response of the voltage control is chosen to be slow in order to allow the action of the synthetic inertia: if ω_{c-vdc} were to be chosen high, the voltage across the capacitor C_{dc} would change too quickly, preventing it from storing/delivering energy during frequency transients.

The model associated to the DC voltage control is reported in Figure 3.5 in which the internal current loop has been approximated as a first order transfer function $K_I(s)$ with cut-off angular frequency $\omega_{cI} = 40\,rad/s$ and the control plant is represented by the block $F_{dc}(s)$:

$$K_I(s) = \frac{L_I(s)}{1 + L_I(s)} \cong \frac{\omega_{cI}}{s + \omega_{cI}} \tag{3.15}$$

$$F_{dc}(s) = \frac{1}{I_L(1-D) - \frac{s\,C_{dc}V_{dc}}{\omega_{b-dc}}} \tag{3.16}$$

The following assumptions for the steady state variables have been made:

- $I_L(1-D) = I_{dc} \in [0;1] p.u.$;
- $V_{dc} = V_{dc-ref} = 1\,p.u$;
- $\omega_{b-dc} = 1\,rad/s$.

The equivalent load function $G_{dc1}(s)$ can be identified from Figure 3.5: it is characterized by the pole in ω_{cI} and by an unstable pole introduced by the linear model of the DC-Bus:

$$G_{dc1}(s) = K_I(s) \cdot F_{dc}(s) = \frac{\omega_{cI}}{(s+\omega_{cI})} \cdot \frac{-\frac{1}{C_{dc}V_{dc}}}{\left(s - \frac{I_{dc}}{C_{dc}V_{dc}}\right)} \tag{3.17}$$

Moreover, Figure 3.5 shows the presence of a disturbance Δi_{dc} generated by the variation of the PV source current: normally this disturbance is associated to slow dynamics and has a negligible effect.

Equation (3.17) shows the influence of the PV source current I_{dc} on the unstable pole: assuming no current is being injected ($I_{dc} = 0$), the equivalent load function includes a natural integral associated to the capacitor dynamics; on the other hand, for increasing current injections, the magnitude of $G_{dc}(s)$ decreases. The Bode diagram of $G_{dc}(s)$ is shown in Figure 3.6, highlighting the influence of the current injection. The most critical case for the control system occurs when the current injection is maximum ($I_{dc} = 1\ p.u.$).

The double-loop architecture has been chosen to overcome the instability of $F_{dc}(s)$: the inner regulator $R_{dc1}(s)$ is responsible for the stabilization of the loop function; the outer loop regulator $R_{dc2}(s)$ will provide the desired cut-off frequency and stability margins.

The design of the PI controllers $R_{dc1}(s), R_{dc2}(s)$ will be carried out adopting the conservative hypothesis of $I_{dc} = 1\ p.u.$:

$$R_{dc1}(s) = k_{p-dc1} \cdot \frac{s + z_{dc1}}{s + p_{dc1}} \tag{3.18}$$

$$R_{dc2}(s) = k_{p-dc2} + \frac{k_{i-dc2}}{s} \tag{3.19}$$

For the design of the stabilizing controller $R_{dc1}(s)$, let us consider the open loop transfer function $L_{dc1}(s)$ and the closed loop function $F_1(s)$:

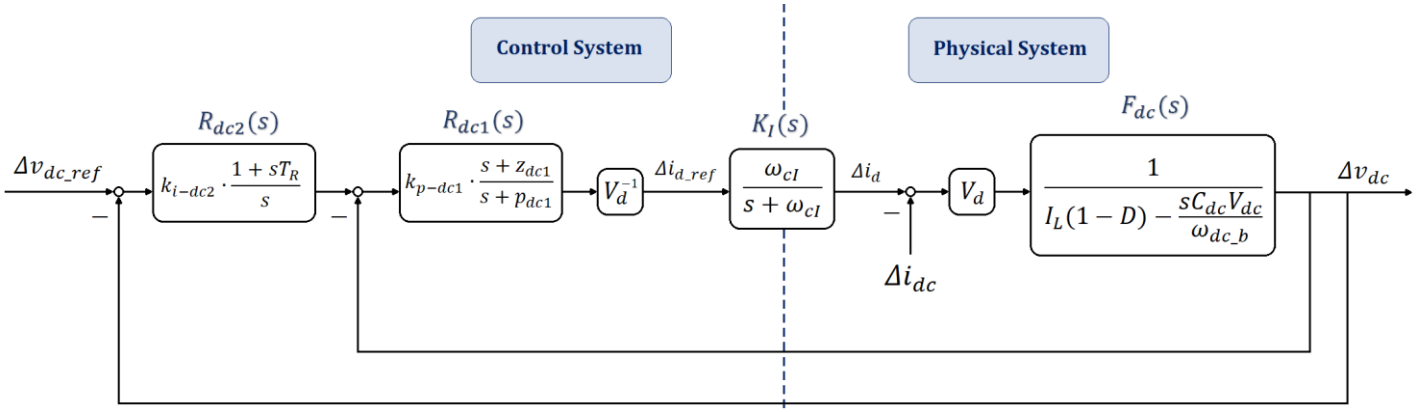

Figure 3.5 – Double loop model associated to the DC voltage loop control.

$$L_{dc1}(s) = R_{dc1}(s) \cdot G_{dc1}(s) = k_{p-dc1} \cdot \frac{s + z_{dc1}}{s + p_{dc1}} \cdot \frac{\omega_{cI}}{(s + \omega_{cI})} \cdot \frac{-\frac{1}{C_{dc}V_{dc}}}{\left(s - \frac{I_{dc}}{C_{dc}V_{dc}}\right)} = \frac{s + z_{dc1}}{s + p_{dc1}} \cdot \frac{\rho \cdot k_{p-dc1}}{(s + \omega_{cI}) \cdot (s - p_1)} \quad (3.20)$$

$$F_1(s) = \frac{L_{dc1}(s)}{1 + L_{dc1}(s)} \quad (3.21)$$

Where $\rho = \frac{-\omega_{cI}}{C_{dc}V_{dc}}$, $p_1 = \frac{I_{dc}}{C_{dc}V_{dc}}$.

The regulator $R_{dc1}(s)$ must be designed so that $den[F_1(s)] = (s + X_A)^2$, where $X_A = 1.2\ rad/s$ has been chosen to account for some margin with respect to the desired cut off frequency $\omega_{c-vdc} = 1\ rad/s$ (Figure 3.7). By considering $z_{dc1} = \omega_{cI}$ it results:

$$L_{dc1}(s) = \frac{\rho \cdot k_{p-dc1}}{(s + p_{dc1}) \cdot (s - p_1)} \quad (3.22)$$

$$den[F_1(s)] = 1 + L_{dc1}(s) = s^2 + s(p_{dc1} - p_1) - p_{dc1}p_1 + \rho \cdot k_{p-dc1} \quad (3.23)$$

The root locus of the feedback loop is shown in Figure 3.7. The position of the unstable pole $p_1$is established by assuming that the system variables can vary within a 10% range around their steady state value. The worst case corresponds to the rightmost value of p_1, which can be obtained by:

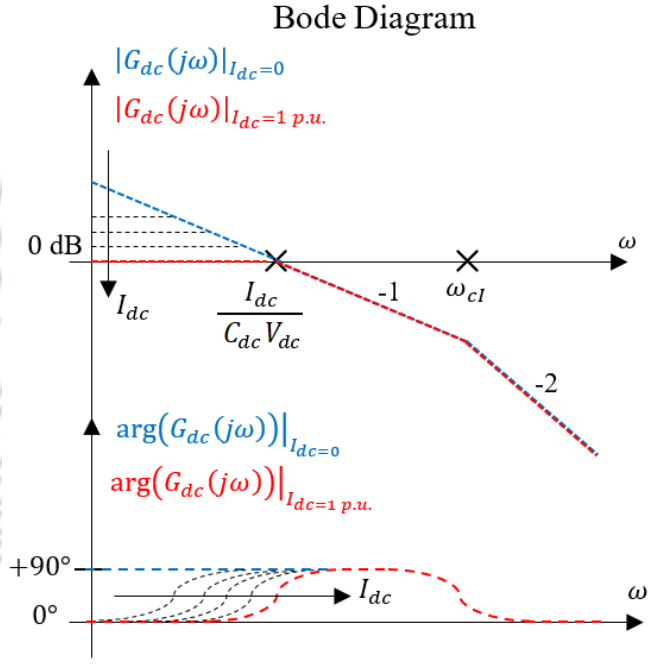

Figure 3.6 – Equivalent load function $G_{dc1}(s)$ associated to the DC-Bus voltage control [5].

$$p_1 \leq p_{1-max} = \frac{I_{dc-max}}{C_{dc} V_{dc-min}} = 36.16\, rad/s \tag{3.24}$$

Considering the denominator of $F_1(s)$ (3.23), the value of the pole p_{dc1} and k_{p-dc1} can be found as follows:

$$2\, X_A = p_{dc1} - p_1 \quad \rightarrow \quad p_{dc1} \geq p_1 + 2X_A = 38.56\, rad/s \tag{3.25}$$

$$-p_{dc1} \cdot p_1 + \rho \cdot k_{p-dc1} = {X_A}^2 \tag{3.26}$$

$$k_{p-dc1} = \frac{{X_A}^2 + p_{dc1} \cdot p_1}{\rho} = -1.214\ p.u. \tag{3.27}$$

As regards the controller $R_{dc2}(s)$, it is designed with reference to function (3.28) and the values of its parameters have been found with MatLab:

$$F_1(s) = \frac{R_{dc1}(s) \cdot G_{dc1}(s)}{1 + R_{dc1}(s) \cdot G_{dc1}(s)} \cong \frac{\rho \cdot k_{p-dc1}}{(s + X_A)^2} \tag{3.28}$$

$$L_{dc}(s) = R_{dc2}(s) \cdot F_1(s) \tag{3.29}$$

Figure 3.8 shows the Bode diagrams and the step response associated to the DC loop.

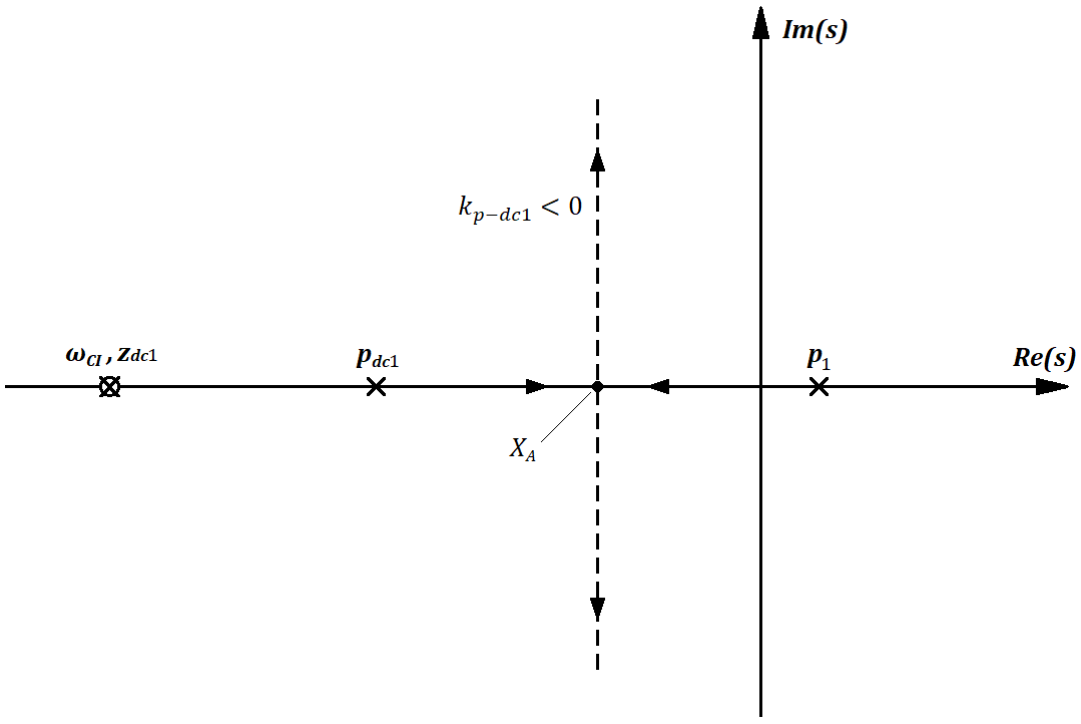

Figure 3.7 – Root locus of the DC-Bus feedback loop

Table 8 – Values of the DC-Bus voltage loop control parameters

Parameter	Symbol	Value
DC-Bus voltage	V_{dc}	750 V
DC-Bus capacitance	C_{dc}	30 mF (@750 V)
Desired cut-off angular frequency	ω_{c-dc}	1 rad/s
$R_{dc1}(s)$	k_{p-dc1}	−1.180 p.u.
	z_{dc1}	40.0 rad/s
	p_{dc1}	38.6 rad/s
$R_{dc2}(s)$	k_{p-dc2}	1.331e−3 p.u.
	k_{i-dc2}	1.133e−3 p.u./s

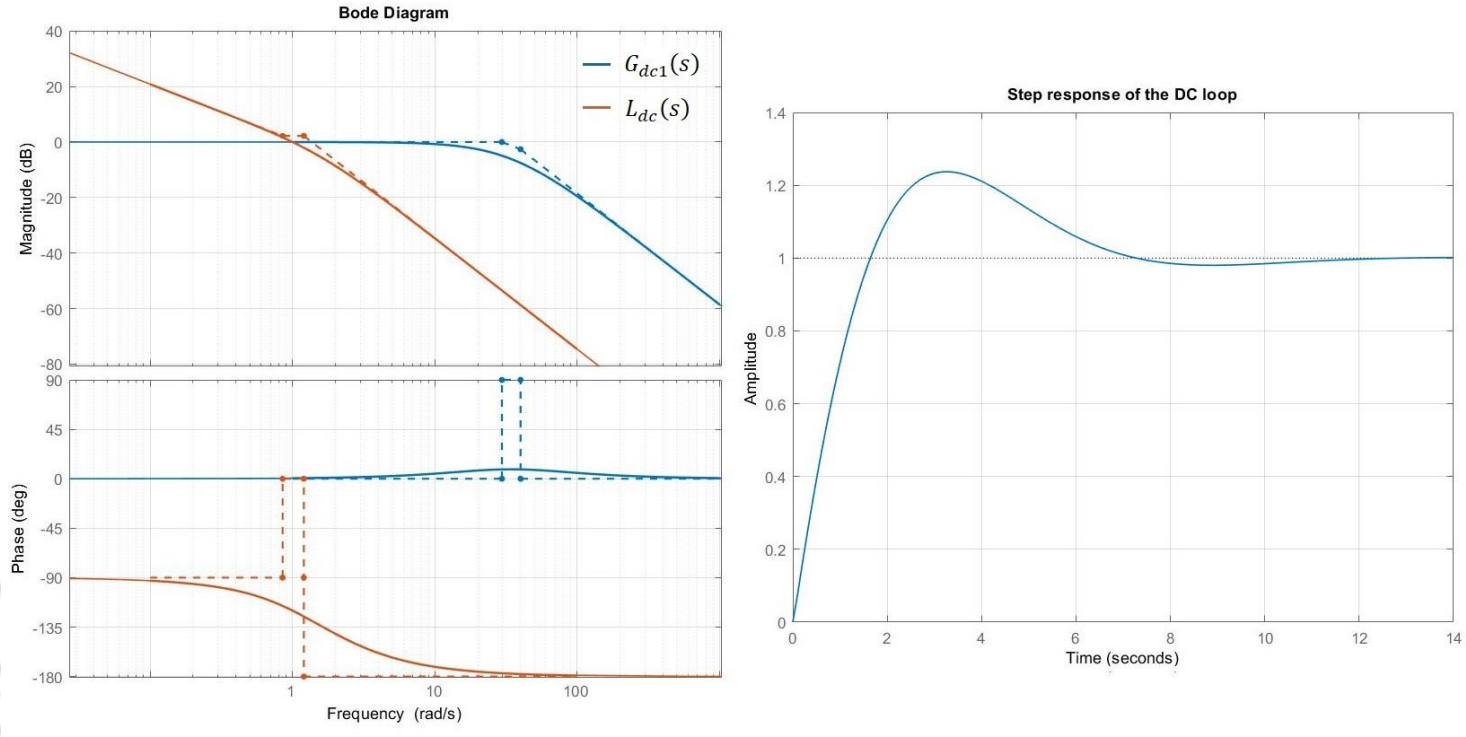

Figure 3.8 – Bode diagrams and step response of the DC voltage control loop.

3.5 MPPT and PV Voltage Control

The small-signal model associated to the MPPT and PV-Bus voltage control loops is reported in Figure 3.9 with the relative PI regulators. The equivalent load function $G_{pv}(s)$ is given by:

$$G_{pv}(s) = \frac{\frac{-\omega_{dc-b}{}^2 V_{dc}}{L_b C_{in}}}{M_1(s)} \tag{3.30}$$

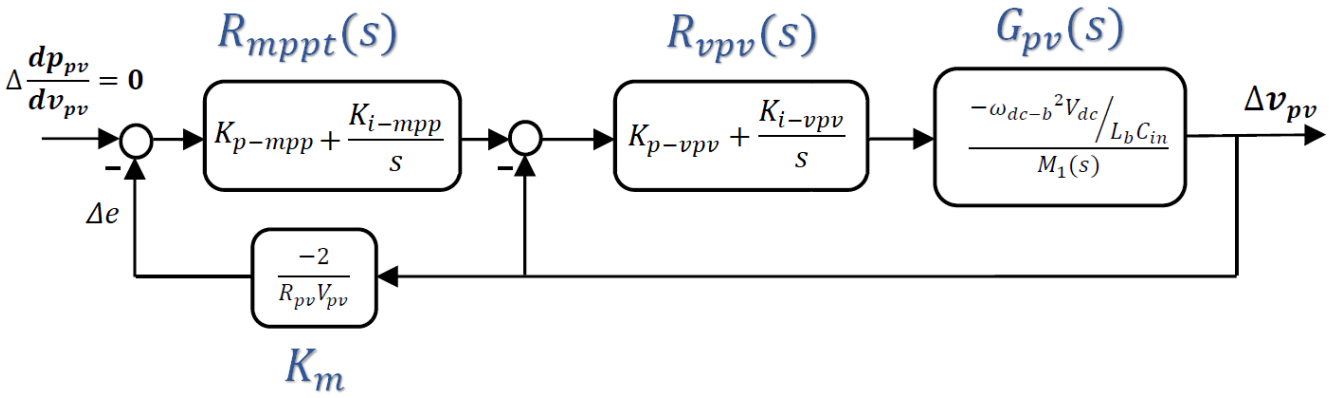

Figure 3.9 – Small-signal model associated to the MPPT and PV-Bus voltage control loops

Where the denominator $M_1(s)$ is defined as:

$$M_1(s) = s^2 + \omega_{dc-b}\left(\frac{r_L}{L_b} + \frac{1}{R_{pv}C_{in}}\right)s + \frac{\omega_{dc-b}{}^2}{L_b C_{in}}\left(\frac{r_L}{R_{pv}} + 1\right) \tag{3.31}$$

and it is characterized by two complex conjugate negative-real part poles at $\omega_p \cong 370\ rad/s$. The open-loop transfer function $L_{pv}(s)$ is obtained from Figure 3.9

$$R_{vpv}(s) = k_{p-vpv} + \frac{k_{i-vpv}}{s} \tag{3.32}$$

$$L_{pv}(s) = R_{vpv}(s) \cdot G_{pv}(s) \tag{3.33}$$

The numerical Bode diagrams associated to $G_{pv}(s)$ and $L_{pv}(s)$ are reported in Figure 3.11 as well as the step response of the closed loop. Figure 3.11 shows that the load function is characterized two complex conjugate poles at $\omega_{M1} = \sqrt{\frac{1}{L_b C_{in}}} \cong 365\ rad/s$. As a consequence, the cut of frequency of the loop needs to be sufficiently smaller to avoid strong oscillations in the step response.

As regards the MPPT algorithm, the incremental conductance method (INC) has been implemented: the input to the MPPT controller is PV voltage and current which is used to generate the reference voltage at which the instantaneous power from the PV array is maximum. The operating point can be estimated from the incremental conductance:

$$\begin{aligned} &\frac{dp_{pv}}{dv_{pv}} = \frac{d(v_{pv} \cdot i_{pv})}{dv_{pv}} = i_{pv} + v_{pv}\frac{di_{pv}}{dv_{pv}} \\ &\frac{1}{v_{pv}} \cdot \frac{dp_{pv}}{dv_{pv}} = \frac{i_{pv}}{v_{pv}} + \frac{di_{pv}}{dv_{pv}} \longrightarrow e = \frac{i_{pv}}{v_{pv}} + \frac{di_{pv}}{dv_{pv}} \end{aligned} \tag{3.34}$$

Where the quantity e is expressed as a sum of the actual conductance i_{pv}/v_{pv} and the incremental conductance di_{pv}/dv_{pv}. By linearizing (3.34) around the working point the following expression is obtained (appendix) [10]:

$$e = K_m \cdot v_{pv} \qquad \text{where } K_m = -\frac{2}{R_{pv}V_{pv}} \tag{3.35}$$

As regards the MPPT loop, the diagram of Figure 3.10 can be considered where the load function $G_{mppt}(s)$ and the open loop function $L_{mppt}(s)$ are given by:

$$G_{mppt}(s) = \frac{L_{pv}(s)}{1 + L_{pv}(s)}; \qquad L_{mppt}(s) = K_m \cdot R_{vpv}(s) \cdot G_{mppt}(s) \tag{3.36}$$

The Bode diagram associated to the MPPT loop are reported in Figure 3.11 as well as the step response of the closed loop function.

Table 9 – Parameters of the PI regulator for MPPT and PV-Bus voltage loop

Parameter	Symbol	Value
Desired cut-off angular frequencies	ω_{c-vpv} ω_{c-mppt}	60 rad/s 10 rad/s
Phase margin	PM_{vpv} PM_{mppt}	60° 60°
Proportional coefficients	k_{p-vpv} k_{p-mppt}	$0\ p.u.$ $-58..5\ p.u.$
Integral coefficients	k_{i-vpv} k_{i-mppt}	$0\ p.u./s$ $5.62\ p.u./s$

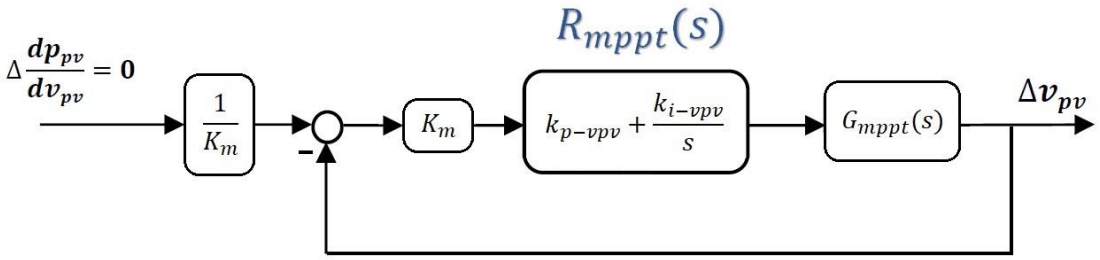

Figure 3.10 – MPPT loop diagram

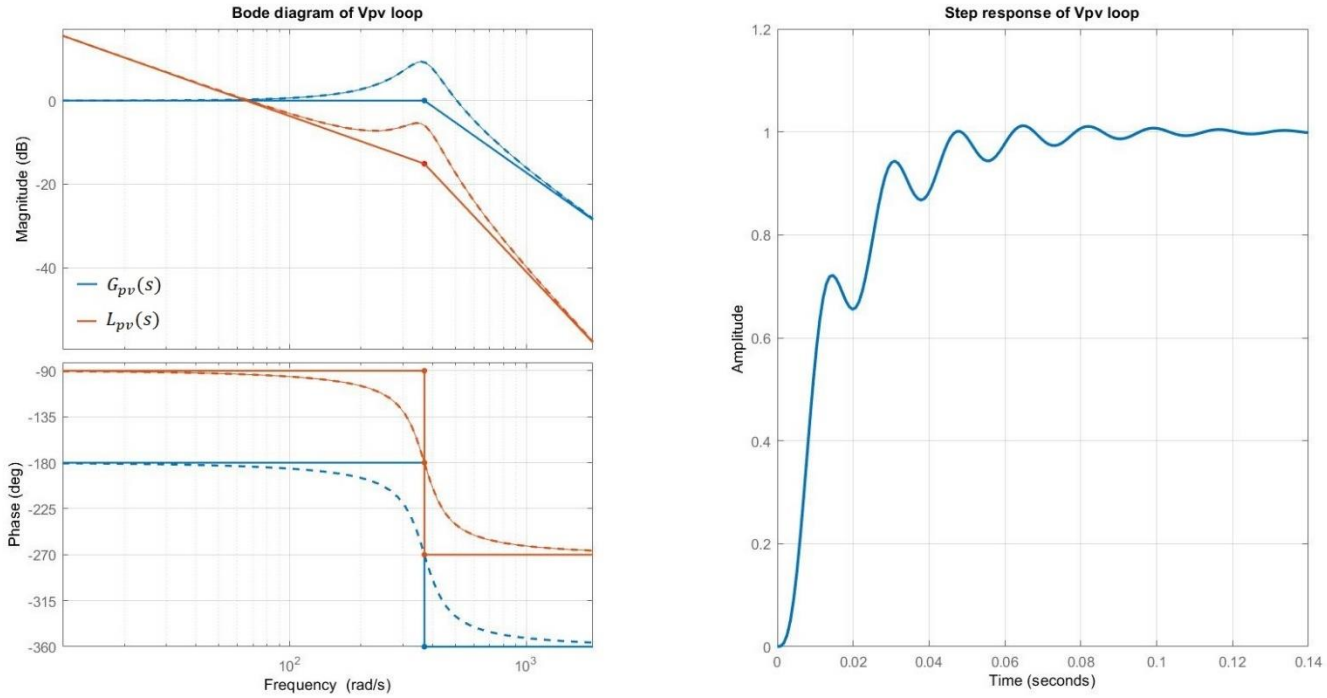

Figure 3.11 – Numerical Bode diagrams of $G_{pv}(s)$, $L_{pv}(s)$ and step response of the PV voltage loop.

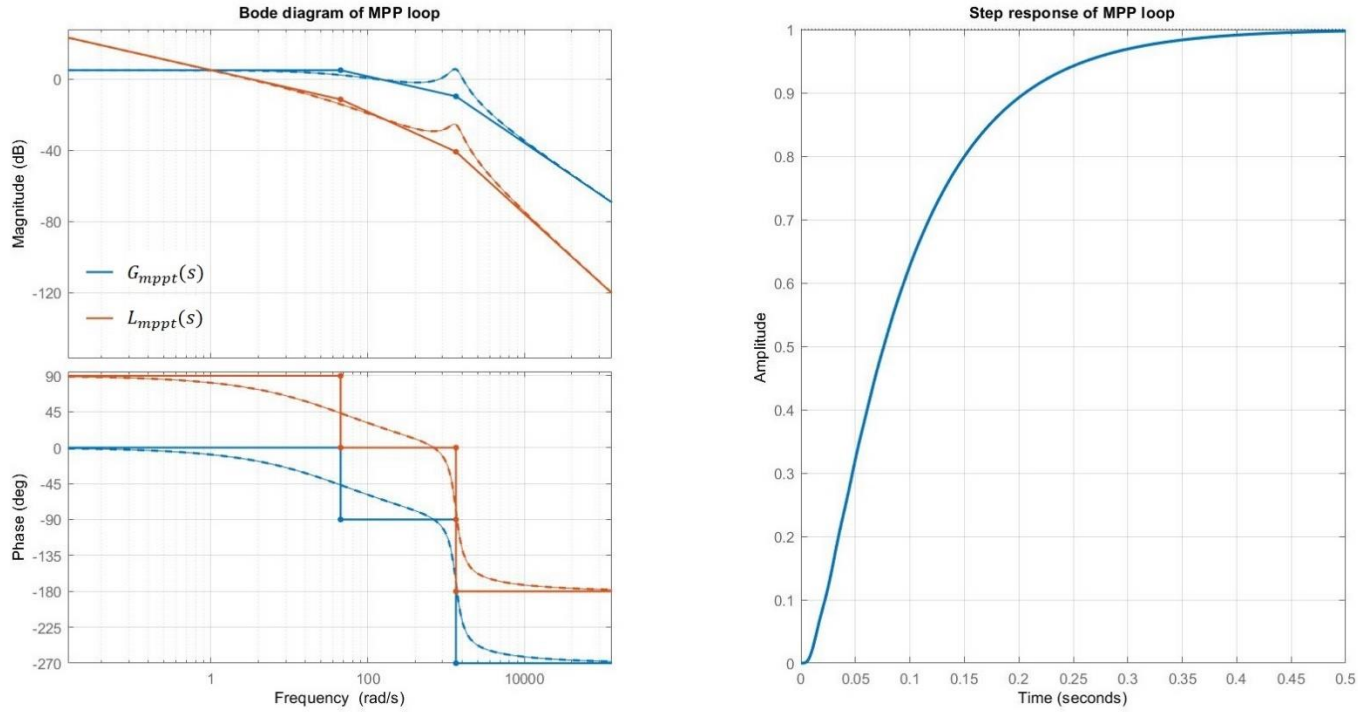

Figure 3.12 – Numerical Bode diagram and step response of the full PV voltage loop.

4. Chapter four

Mathematical Analysis of System Interactions

This chapter is dedicated to the calculation of the most significant transfer functions of the model. In the beginning, some useful simplifications are introduced to simplify the full transfer function diagram (Figure 4.1) obtained in section 2.5, which allow to better understand the interaction between different parts of the system. Later, considering the step change in load power Δp_g as input, the response of the main transfer functions is analyzed. All the results found in this chapter are valid for the small signal model developed in Chapter two.

4.1 Simplification of Transfer Functions

Considering the numerical values of the parameters found in previous chapters, it is possible to introduce some simplifications to the system transfer functions (Figure 4.1) and consequentially to the overall system diagram. This allows show the interactions between the different parts of the system in a more understandable way.

- Considering $\omega_{c-vdc} = 1\ rad/s$, the current control loop block $K_I(s)$ behaves as a low-pass filter with unitary gain and cut-off frequency $\omega_{CI} = 40\ rad/s$ and thus can be approximated to its gain value for frequencies lower than ω_{CI}.

$$K_I(s) = \frac{1}{1 + s/\omega_{CI}} \approx 1\ p.u., \quad for\ \omega < \omega_{CI} \tag{4.1}$$

- The blocks $G_a(s)$, $G_{pv}(s)$ determine the PV-Bus voltage variation Δv_{pv}. Considering $\sigma = {\omega_{b-dc}}^2 / L_b C_{in} \cong 1.33 \cdot 10^5\ rad^2/s^2$, they can be written as:

$$G_a(s) = \frac{\Delta v_{pv}}{\Delta v_{dc}} = \frac{\sigma\,(1-D)}{M_1(s)} \tag{4.2}$$

$$G_{pv}(s) = \frac{\Delta v_{pv}}{\Delta d} = \frac{-\sigma\, V_{dc}}{M_1(s)} \tag{4.3}$$

Where the denominator $M_1(s)$ is a second order polynomial with double complex-conjugate poles, which can be approximated as in (4.4):

$$M_1(s) = s^2 + \omega_{b-dc}\left(\frac{r_L}{L_b} + \frac{1}{R_{pv}C_{in}}\right)s + \sigma\left(\frac{r_L}{r_{pv}} + 1\right) \approx s^2 + \frac{\omega_{b-dc}}{R_{pv}C_{in}}s + \sigma \tag{4.4}$$

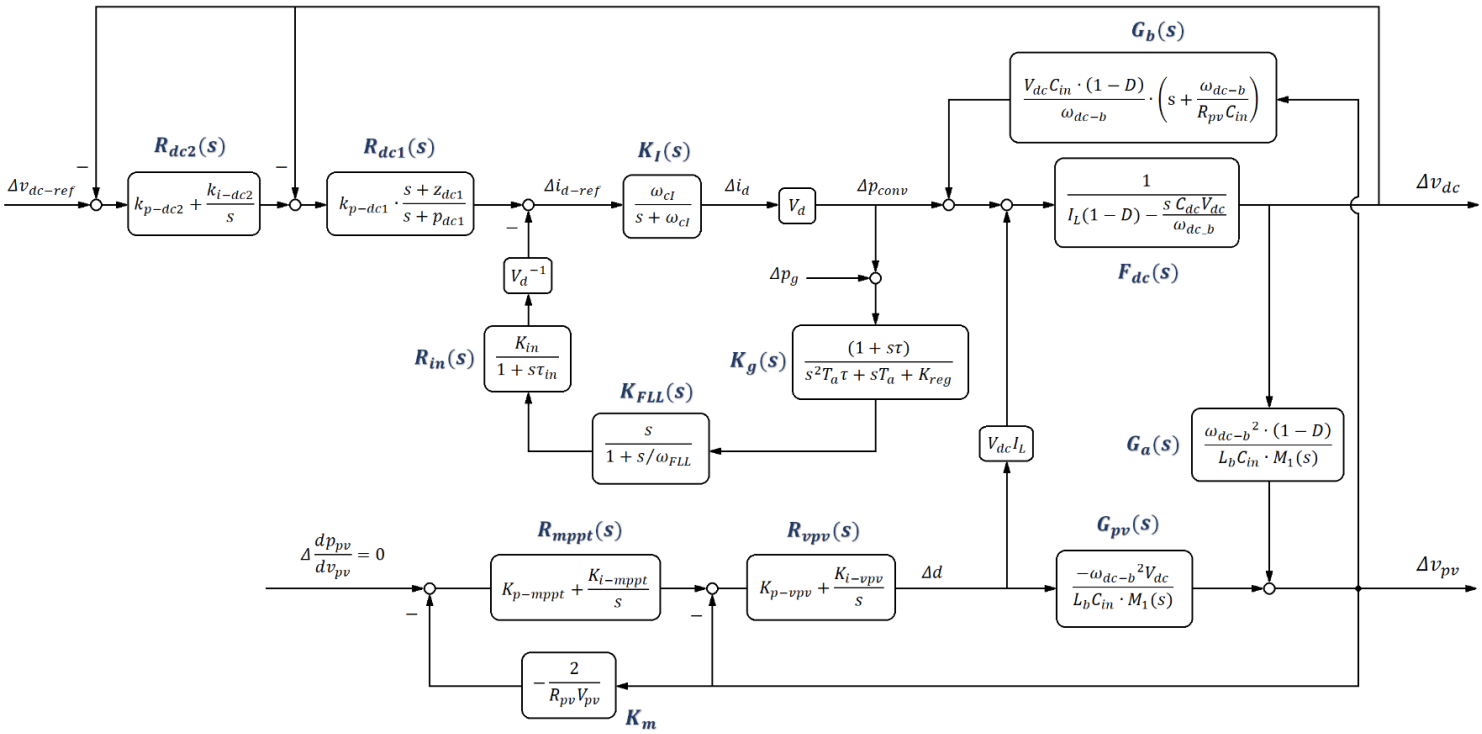

Figure 4.1 – Full system transfer function diagram

Where: $\frac{r_L}{L_b} \ll \frac{1}{r_{pv}C_{in}}$; $\frac{r_L}{r_{pv}} \ll 1$ p.u..

The natural frequency of $M_1(s)$ is $\omega_{M1} = \sqrt{\frac{1}{L_bC_{in}}} \cong 365\,rad/s$, therefore at low frequencies it can be approximated as $M_1(s) \approx \sigma$, for $\omega < \omega_{M1}$. The expressions (4.2) and (4.3) can be rewritten as:

$$G_a(s) \approx (1-D) \qquad \text{for } \omega < \omega_{M1} \tag{4.5}$$

$$G_{pv}(s) \approx -V_{dc} \tag{4.6}$$

- Considering the block $G_b(s)$:

$$G_b(s) = \frac{V_{dc}C_{in}\cdot(1-D)}{\omega_{b-dc}}\cdot\left(s+\frac{\omega_{b-dc}}{r_{pv}C_{in}}\right) \tag{4.7}$$

It has a zero in $\omega_z = \left|-\frac{1}{r_{pv}C_{in}}\right| \cong 128\,rad/s$, therefore for $\omega < \omega_z$ it can be approximated to its gain value:

$$G_b(s\to 0) = \frac{V_{dc}(1-D)}{r_{pv}} \cong 0.5786\,p.u. \tag{4.8}$$

The numerical values used for simplifications are reported in Table 10.

Table 10 – Per-unit values of the parameters used for simplifications

Parameter	Value [p.u.]
L_b	$1.3 \cdot 10^{-3}$
C_{in}	$5.6 \cdot 10^{-3}$
r_L	$17.8 \cdot 10^{-6}$
r_{pv}	1.39

4.2 Simplification of the Model

As regards the reference signals, when the system operates at steady-state and the PV source works at MPP, the following relations are valid:

$$\begin{aligned} \Delta v_{dc-ref} &= 0 \\ \Delta \frac{dp_{pv}}{dv_{pv}} &= 0 \end{aligned} \tag{4.9}$$

This allows to consider the regulators of V_{pv} and V_{dc} loop as two single blocks and simplify the full block diagram as shown in Figure 4.2.

$$\begin{aligned} R_{dc}(s) = -R_{dc1}(s) \cdot [1 + R_{dc2}(s)] &= -k_{p-dc1} \cdot \frac{s + z_{dc1}}{s + p_{dc1}} \cdot \left[\frac{s(1 + k_{p-dc2}) + k_{i-dc2}}{s}\right] \\ &= -k_{p-dc1}\left[\frac{(s + z_{dc1})(s + k_{i-dc2})}{s(s + p_{dc1})}\right] = -k_{p-dc1}\frac{s^2 + z_{dc1}s + z_{dc1}k_{i-dc2}}{s(s + p_{dc1})} \end{aligned} \tag{4.10}$$

Where: $k_{p-dc2} \ll 1$; $k_{i-dc2} \ll z_{dc1}$.

$$\begin{aligned} R_{pv}(s) = -R_{vpv}(s) \cdot \left[1 + k_m R_{mpp}(s)\right] &= -\left(\frac{k_{i-vpv}}{s}\right) \cdot \left[1 + \frac{k_m k_{i-mpp}}{s}\right] \\ &= -k_{i-vpv}\frac{s + k_m k_{i-mpp}}{s^2} \end{aligned} \tag{4.11}$$

To analyze the interaction between the load power change Δp_g and the DC-Bus voltage change Δv_{dc} the following relations can be deduced from the simplified diagram of Figure 4.2:

$$\Delta v_{pv} = G_a(s) \cdot \Delta v_{dc} + G_{pv}(s) \cdot \Delta d \tag{4.12}$$

$$\Delta d = R_{pv}(s) \cdot \Delta v_{pv} \tag{4.13}$$

Substituting (4.13) into (4.12) and solving for Δv_{pv} results in (4.15):

$$\Delta v_{pv} = G_a(s) \cdot \Delta v_{dc} + R_{pv}(s) \cdot G_{pv}(s) \cdot \Delta v_{pv} \tag{4.14}$$

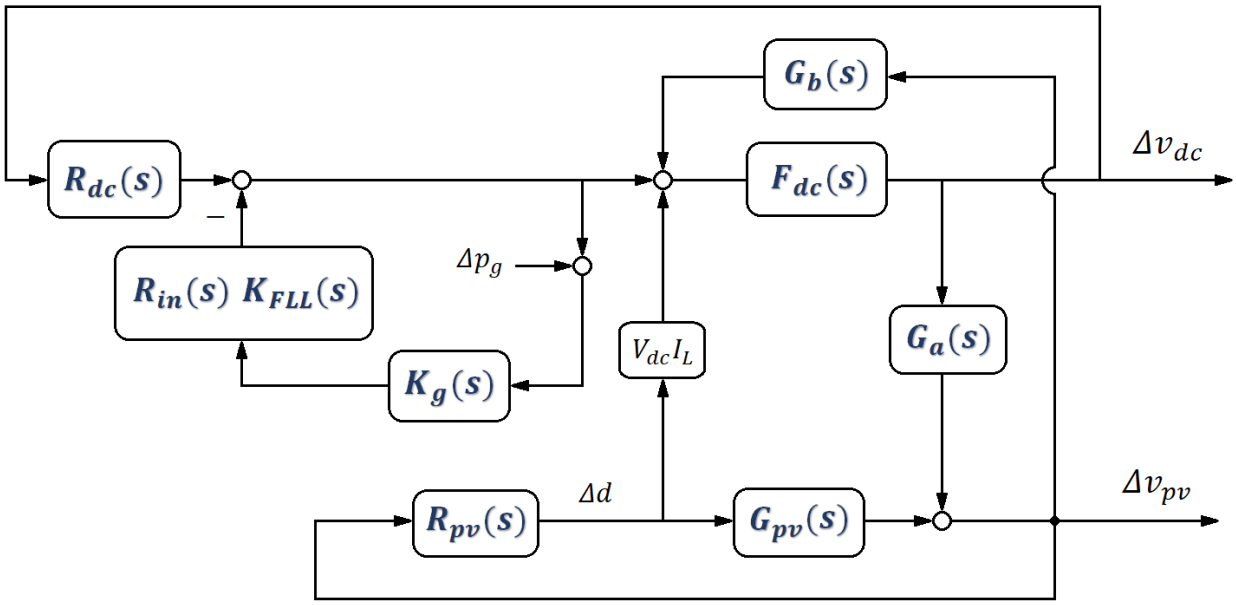

Figure 4.2 – Simplified transfer function diagram.

$$\Delta v_{pv} = \frac{G_a(s)}{1 - R_{pv}(s) \cdot G_{pv}(s)} \cdot \Delta v_{dc} \tag{4.15}$$

From which the block $G_c(s)$ can be defined:

$$G_c(s) \triangleq \frac{\Delta v_{pv}}{\Delta v_{dc}} = \frac{G_a(s)}{1 - R_{pv}(s) \cdot G_{pv}(s)} \tag{4.16}$$

The simplified block diagram for $\omega < \omega_{CI}$ is reported in Figure 4.3, where the block $G_d(s)$ has been introduced:

$$G_d(s) \triangleq G_b(s) + V_{dc}I_L \cdot R_{pv}(s) \tag{4.17}$$

These simplifications highlight the effects of the DC-Bus voltage variations Δv_{dc} on the PV-Bus voltage Δv_{pv} through $G_c(s)$. It is also shown how Δv_{pv} impacts Δv_{dc} as a disturbance through the block $G_d(s)$.

4.2.1 Analysis of $G_c(s)$ and $G_d(s)$

To analyze $G_c(s)$ and $G_d(s)$, it is useful to rewrite $R_{pv}(s)$ in a more compact form:

$$R_{pv}(s) = \mu \frac{(s + z_{pv})}{s^2} \tag{4.18}$$

Where μ is the static gain and z_{pv} is the zero of $R_{pv}(s)$:

$$z_{pv} = -k_m k_{i-mpp} = -10.13\ rad/s$$
$$\mu = -k_{i-vpv} = 58.53\ p.u. \tag{4.19}$$

$$G_c(s) = \frac{G_a(s)}{1 - R_{pv}(s)\cdot G_{pv}(s)} = \frac{G_a(s)}{1 + \mu\dfrac{(s + z_{pv})}{s^2}}; \qquad with: G_{pv}(s) = -V_{dc} = -1\ p.u. \tag{4.20}$$

$$G_c(s) = \frac{s^2(1-D)}{s^2 + \mu\, s + \mu\, z_{pv}}$$

$G_c(s)$ has two zeros in the origin $(z_{Gc1}, z_{Gc2} = 0)$ and two poles that can be found as:

$$p_{Gc1}, p_{Gc2} = \frac{-\mu \pm \sqrt{\mu^2 - 4\,\mu\, z_{pv}}}{2}$$
$$p_{Gc1} = -13.03\ rad/s \tag{4.21}$$
$$p_{Gc2} = -45.50\ rad/s$$

As regards $G_d(s)$:

- $$G_d(s) \triangleq G_b(s) + V_{dc} I_L \cdot R_{pv}(s) = \frac{(1-D)}{r_{pv}} + V_{dc} I_L \cdot \mu \frac{(s + z_{pv})}{s^2}$$
$$= \frac{(1-D)}{r_{pv}}\left[1 + \mu' \frac{(s + z_{pv})}{s^2}\right];\ where\ \ \mu' = \mu \frac{V_{dc} I_L\, r_{pv}}{(1-D)} = 0.5786\ p.u. \tag{4.22}$$

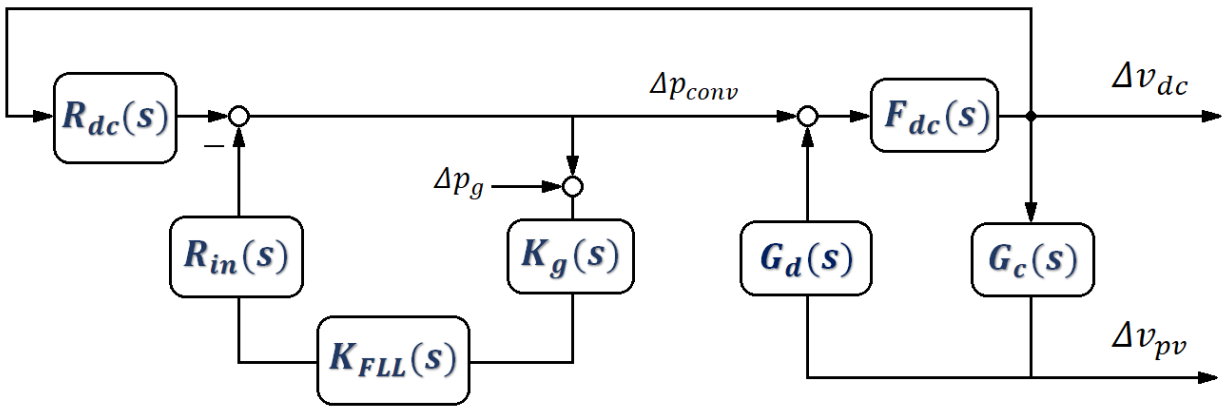

Figure 4.3 – Simplified block diagram for $\omega < \omega_{CI}$.

It has two poles in the origin (p_{Gd1},$p_{Gd2} = 0$) and two zeros which can be calculated as:

$$z_{Gd1},z_{Gd2} = \frac{-\mu' \pm \sqrt{(\mu')^2 - 4\,\mu'\,z_{pv}}}{2} \tag{4.23}$$

$$z_{Gd1} = -11.11\ rad/s$$

$$z_{Gd2} = -115.0\ rad/s$$

The asymptotic Bode diagrams and the zero-pole map of $G_c(s)$ and $G_d(s)$ are reported in Figure 4.4 and Figure 4.5 respectively.

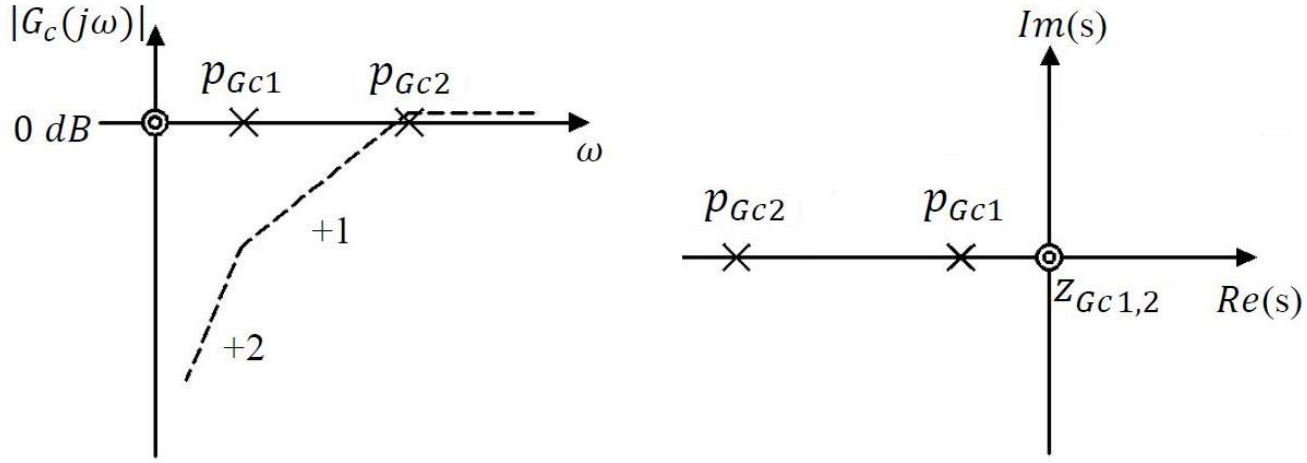

Figure 4.4 – Asymptotic Bode diagram of $G_c(s)$ and zero-pole map

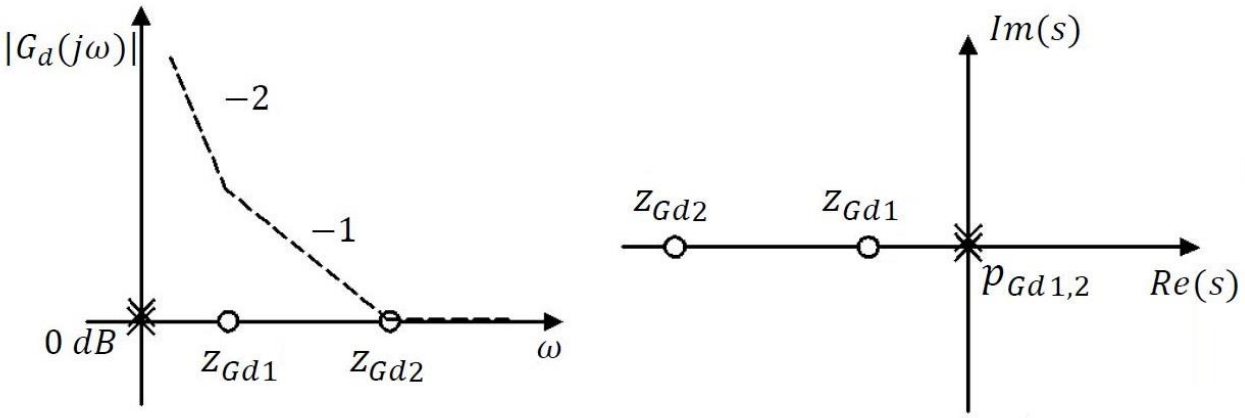

Figure 4.5 – Asymptotic Bode diagram of $G_d(s)$ and zero-pole map

Finally, it is useful to analyze the series of $G_c(s)$ and $G_d(s)$ which constitutes a positive feedback loop to the block $F_{dc}(s)$:

$$G_e(s) = G_c(s) \cdot G_d(s) \tag{4.24}$$

The low frequency zero of $G_d(s)$ is very close to the low frequency pole of $G_c(s)$ and therefore they cancel each other out. Thus, at low frequencies the block $G_e(s)$ can be approximated to its gain value:

$$G_e(s) \approx 0.4642 \tag{4.25}$$

To observe the DC-Bus voltage variations it is useful to define the block $E_{dc}(s)$ as:

$$E_{dc}(s) \triangleq \frac{\Delta v_{dc}}{\Delta p_{conv}} = \frac{F_{dc}(s)}{1 - G_e(s) \cdot F_{dc}(s)} \tag{4.26}$$

4.3 Analysis of the Results

This section is dedicated to the analysis of the step response of the system variables for two different cases:

- Case A: $\Delta p_g = -0.25\, p.u.$
- Case B: $\Delta p_g = +0.25\, p.u.$

According to the conventions used in the transfer function diagram and in Figure 2.8, case A represents an increase of load power absorption and case B a decrease.

4.3.1 Calculation of $\Delta v_{dc}/\Delta p_g$

The transfer function of $\Delta v_{dc}/\Delta p_g$ (4.27) is deduced from the diagram of Figure 4.7.

$$T_{vdc-pg}(s) = \frac{\Delta v_{dc}}{\Delta p_g} = -\frac{E_{dc}(s) \cdot R_{in}(s) \cdot K_g(s) \cdot K_{FLL}(s)}{1 - E_{dc}(s) \cdot R_{dc}(s) + K_g(s) \cdot K_{FLL}(s) \cdot R_{in}(s)} \tag{4.27}$$

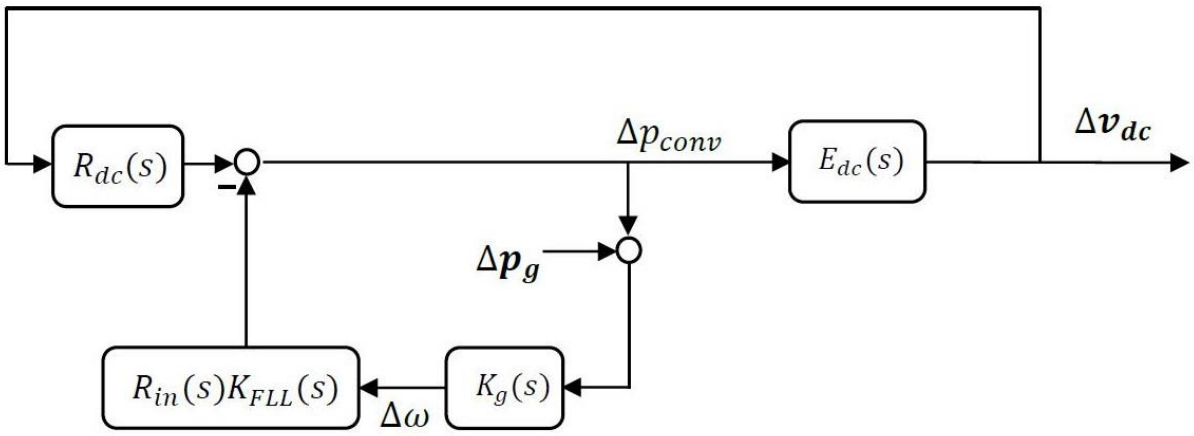

Figure 4.6 – Simplified block diagram with $E_{dc}(s)$

The step response of $T_{vdc-pg}(s)$ is shown in Figure 4.8 for case A: the voltage of the DC-Bus decreases quickly to allow the provision of synthetic inertia by partially discharging the capacitor C_{dc}, and slowly settles back to its nominal value. The step response for case B is shown in Figure 4.9: the DC bus voltage increases to store more energy in the capacitor C_{dc}. As it will be shown in the following sections, these characteristics help damping the grid frequency transient.

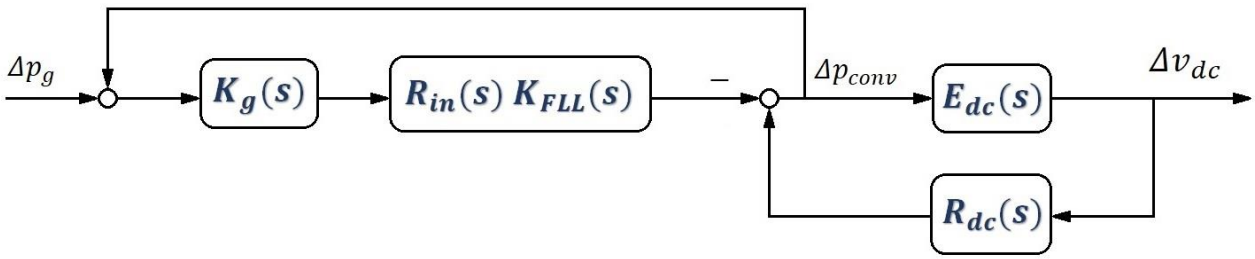

Figure 4.7 - Simplified transfer function diagram for $\Delta v_{dc}/\Delta p_g$ analysis

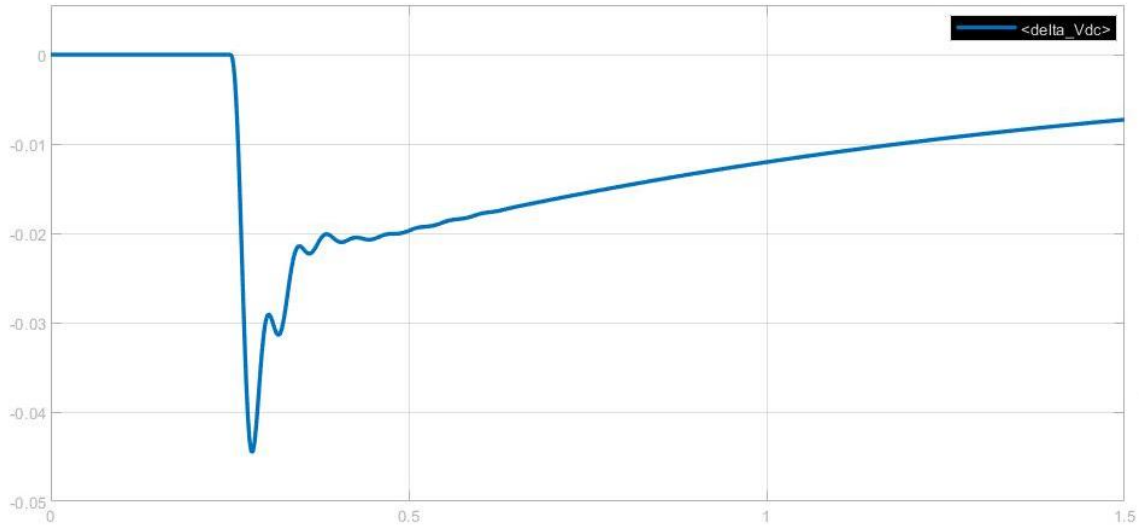

Figure 4.8 – Step response of $\Delta v_{dc}/\Delta p_g$ for case A.

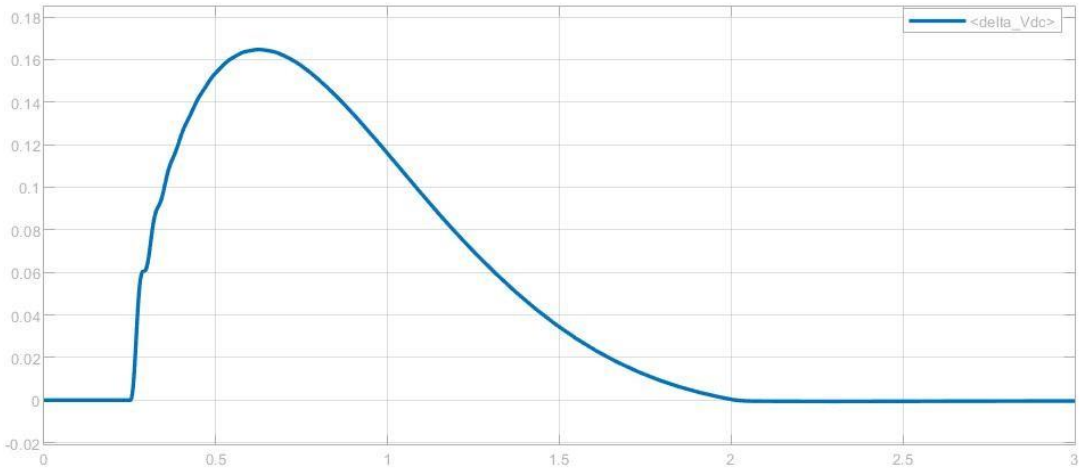

Figure 4.9 – Step response of $\Delta v_{dc}/\Delta p_g$ for case B.

4.3.2 Calculation of $\Delta p_{conv}/\Delta p_g$ and $\Delta p_{pv}/\Delta p_g$

To analyze the influence of a power load variation on the total power delivered by the PQ converter, that is the power delivered by the PV source plus the power delivered by the DC-Bus capacitor (from SIC), let us observe the transfer function $\Delta p_{conv}/\Delta p_g$:

$$T_{pconv-pg}(s) = \frac{\Delta p_{conv}}{\Delta p_g} = \frac{T_{vdc-pg}(s)}{E_{dc}(s)} = -\frac{R_{in}(s)\cdot K_g(s)\cdot K_{FLL}(s)}{1 - E_{dc}(s)\cdot R_{dc}(s) + K_g(s)\cdot K_{FLL}(s)\cdot R_{in}(s)} \tag{4.28}$$

The step response of $T_{pconv-pg}(s)$ is reported in Figure 4.10 for case A and in Figure 4.11 for case B. the results show that in both cases the transients follow the trend of Δv_{dc}.

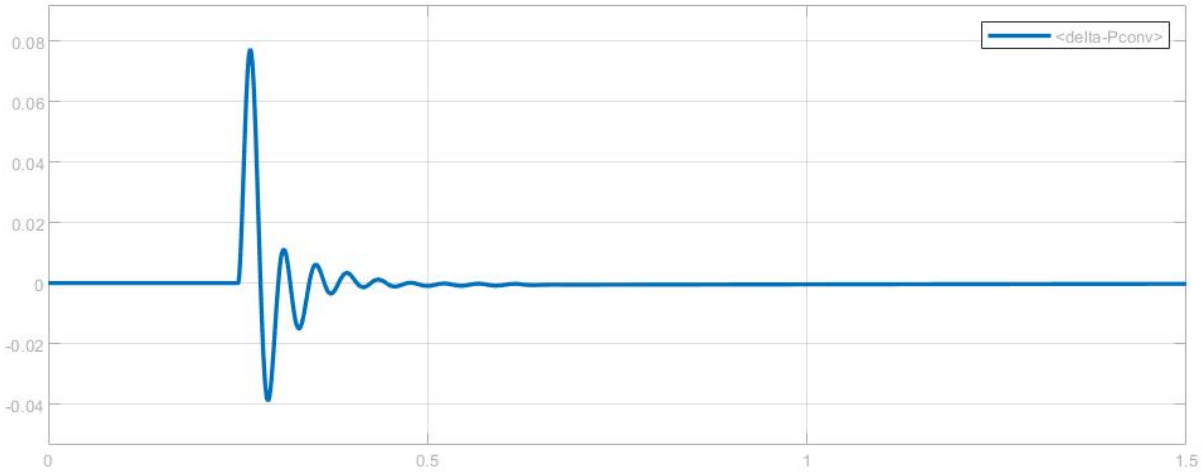

Figure 4.10 – Step response $\Delta p_{conv}/\Delta p_g$ for case A.

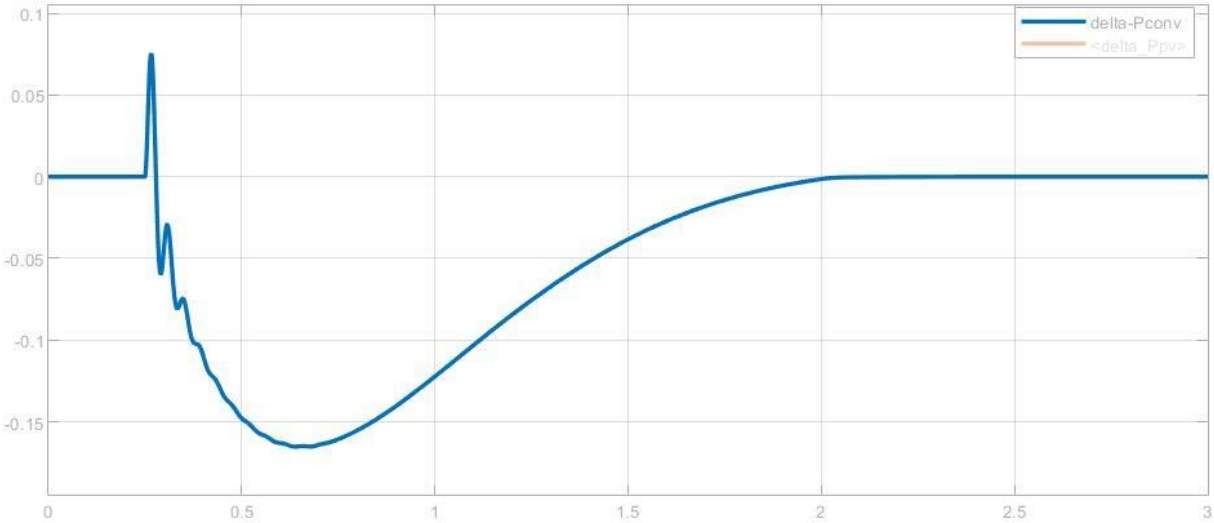

Figure 4.11 – Step response $\Delta p_{conv}/\Delta p_g$ for case B.

As regards the PV power variation Δp_{pv}, its expression can be found by starting from the transfer function $T_{vpv-pg}(s) = \Delta v_{pv}/\Delta p_g$. Considering equations (4.16) and (4.27), this function allows to analyze the variations of the working point of the PV panel due to a change in power load:

$$\begin{aligned} T_{vpv-pg}(s) &= \frac{\Delta v_{pv}}{\Delta p_g} = G_c(s) \cdot \frac{\Delta v_{pv}}{\Delta p_g} = G_c(s) \cdot T_{vdc-pg}(s) \\ &= -\frac{G_c(s) \cdot E_{dc}(s) \cdot R_{in}(s) \cdot K_g(s) \cdot K_{FLL}(s)}{1 - E_{dc}(s) \cdot R_{dc}(s) + K_g(s) \cdot K_{FLL}(s) \cdot R_{in}(s)} \end{aligned} \tag{4.29}$$

The step response of $T_{vpv-pg}(s)$ is reported in Figure 4.12 for case A and in Figure 4.13 for case B.

To obtain the power variation it is necessary to multiply $T_{vpv-pg}(s)$ by the current delivered the PV source according to its static model:

$$T_{ppv-pg}(s) = \frac{\Delta p_{pv}}{\Delta p_g} = \left(I_L + \frac{V_{pv}}{r_{pv}}\right) \cdot T_{vpv-pg}(s) \tag{4.30}$$

Note that, before the load power variation occurs, it is assumed that the system operates at steady state and under nominal conditions, therefore the PV source is operating at MPP. For this reason, it is necessary to impose the condition $\Delta p_{pv} \leq 0, \forall\, \Delta v_{pv}$.

The step response of $T_{ppv-pg}(s)$ is reported in Figure 4.14 for case A and in Figure 4.15 for case B. These results show that v_{pv} decreases rapidly, similarly to v_{dc}, but it quickly recovers thanks to the faster control. Moreover, any oscillation around the nominal value, results in a decrease of the power p_{pv}.

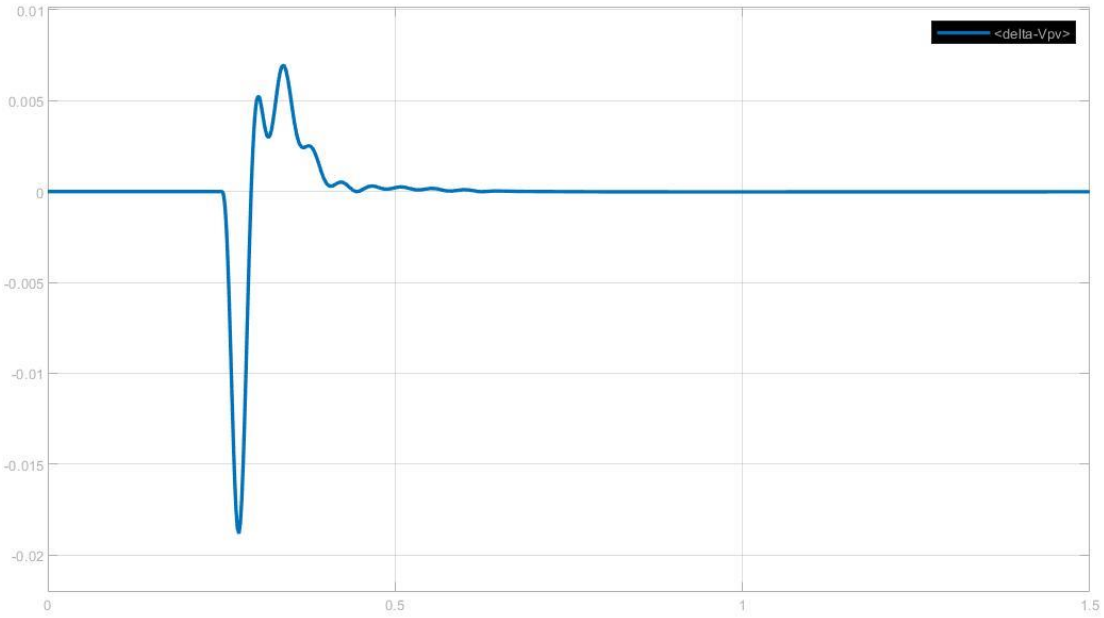

Figure 4.12 – Step response of $\Delta v_{pv}/\Delta p_g$ for case A.

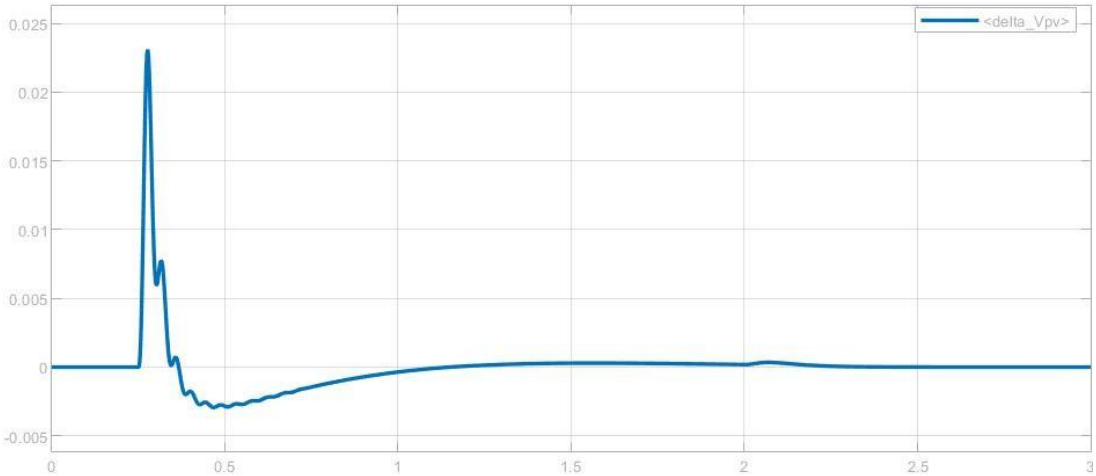

Figure 4.13 – Step response $\Delta v_{pv}/\Delta p_g$ for case B.

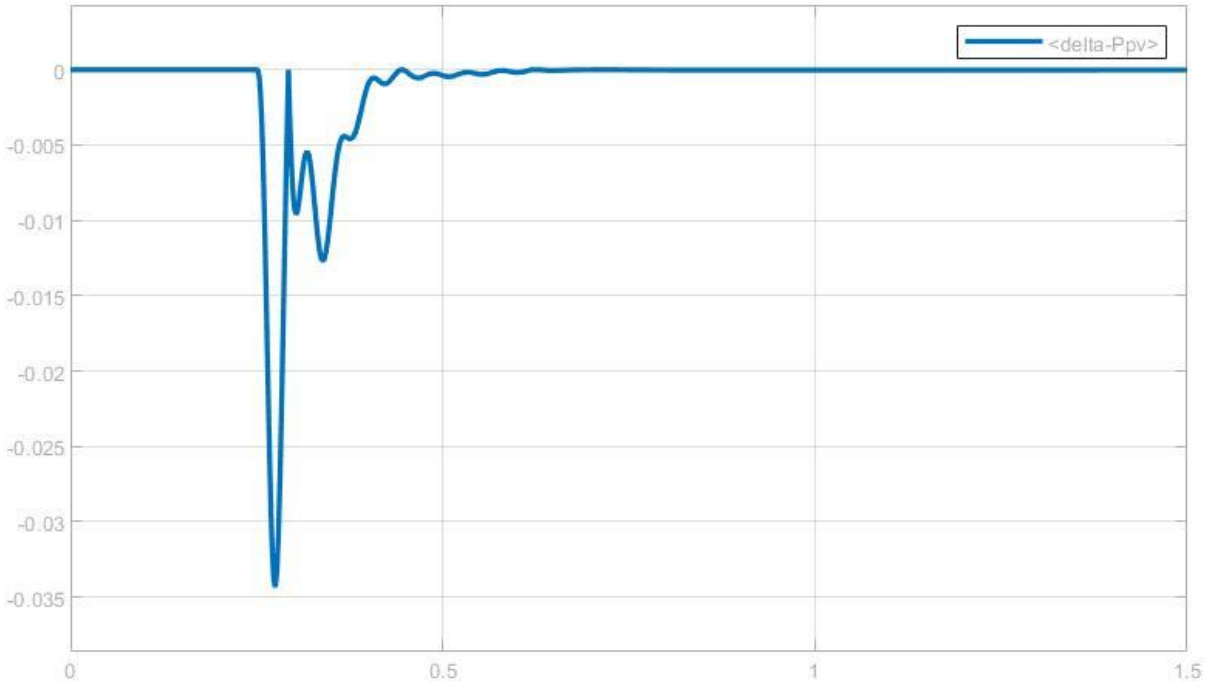

Figure 4.14 – Step response of $\Delta p_{pv}/\Delta p_g$ for case A.

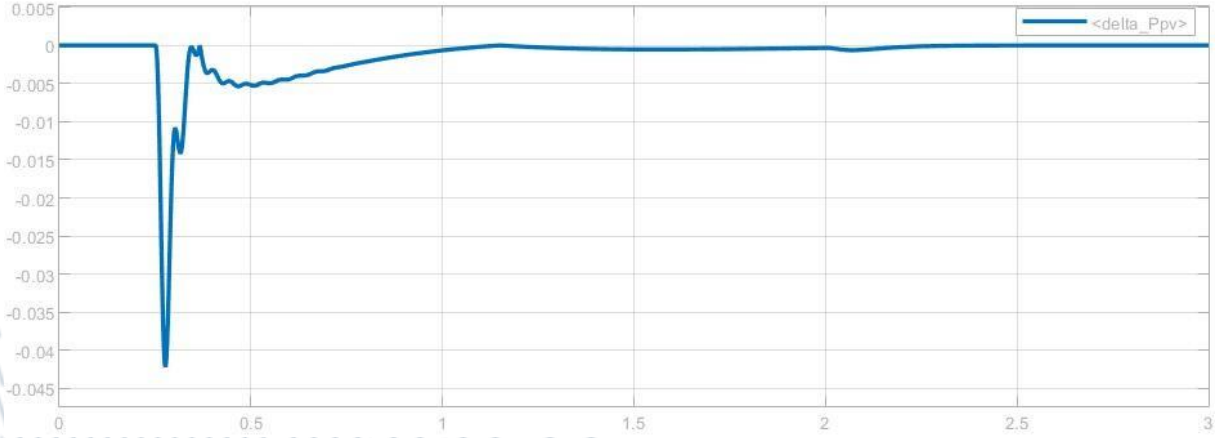

Figure 4.15 – Step response of $\Delta p_{pv}/\Delta p_g$ for case B.

4.3.3 Calculation of $\Delta\omega/\Delta p_g$

The transfer function $\Delta\omega/\Delta p_g$ can be deduced from the diagram of Figure 4.16.

$$T_{\omega-pg}(s) = \frac{\Delta\omega}{\Delta p_g} = \frac{K_g(s)\cdot[1 - E_{dc}(s)\cdot R_{dc}(s)]}{1 - E_{dc}(s)\cdot R_{dc}(s) + K_g(s)\cdot R_{in}(s)\cdot K_{FLL}(s)} \tag{4.31}$$

The block $R_{in}(s)$ is responsible for the provision of synthetic inertia. To clearly visualize its effect on the frequency oscillations, the step response of $T_{\omega-pg}(s)$ has been calculated with $K_{in} = 5\ p.u.$ for the normal case, and $K_{in} = 0$ to represent the absence of inertia provision.

Figure 4.17 and Figure 4.18 show the step response of $T_{\omega-pg}(s)$. The results show that the synthetic inertia provision has a positive effect in reducing the oscillatory response of the transient as well as shortening its duration. However, due to the very small starting time of the grid, the system is not able to dampen significantly the first overshoot of the response which results to be slightly above 3%.

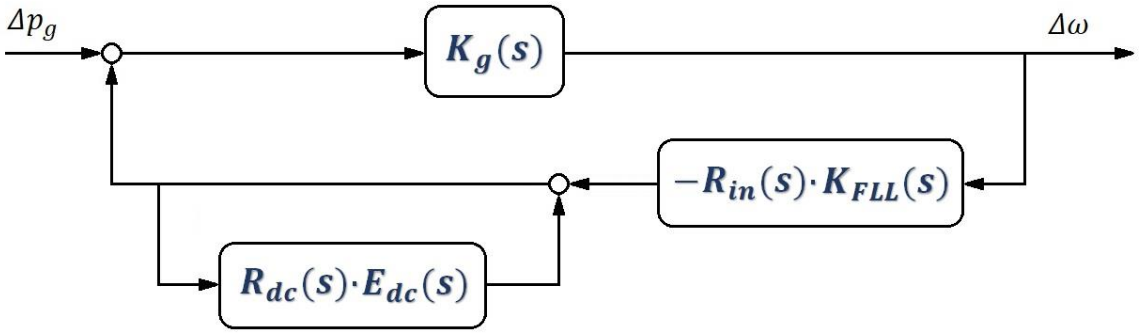

Figure 4.16 – Simplified bode diagram for the calculation of $\Delta\omega/\Delta p_g$.

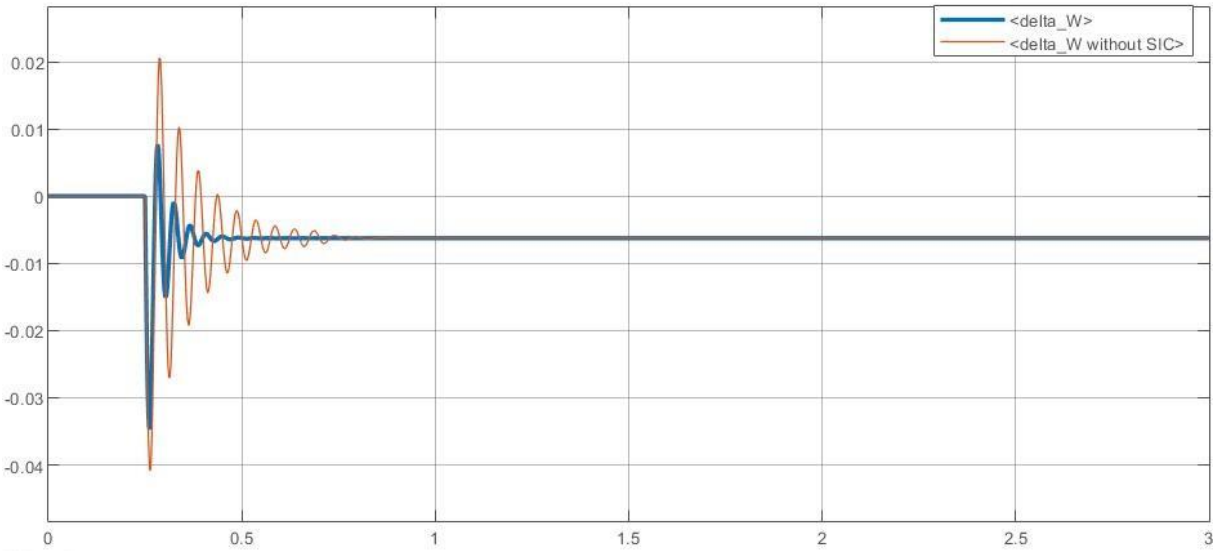

Figure 4.17 – Step response of $\Delta\omega/\Delta p_g$ for case A.

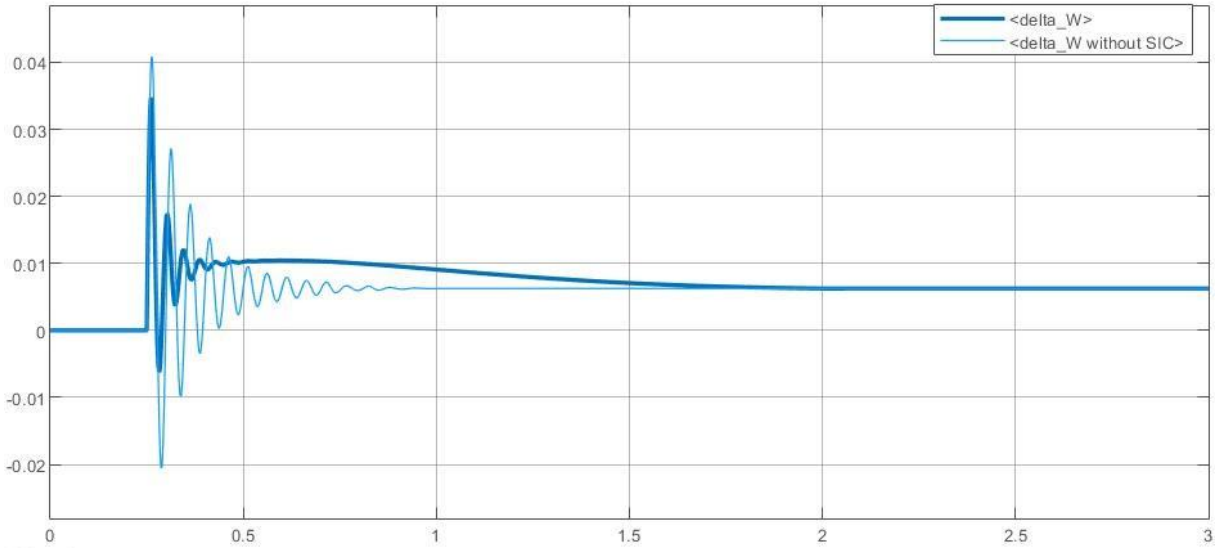

Figure 4.18 – Step response of $\Delta\omega/\Delta p_g$ for case B.

After the transient, the new steady state value of the grid frequency results to be $\pm 0.5\%$ for case A and B, respectively. This is expected since the load increase/decrease is permanent, and the PV system does not change its power output resulting in a grid imbalance.

5. Conclusions

This study has analyzed the interactions between a double-stage PV system equipped with synthetic inertia and a micro-grid characterized by a small starting time in the event of power load variations. The goal was to verify if the results found in previous studies still hold in a more critical case for the whole system.

The mathematical model of the been developed by writing the differential equations and then by deriving the small signal model around the working point. Furthermore, the system has been simplified to highlight the interactions between the PV source, the conversion system, and the external grid.

It is shown that for this system, the provision of synthetic inertia has positive effects on the frequency transients nonetheless, both in terms of the reduction of the overshoot and the shortening of the oscillations.

Bibliography

[1] *Schaber K., Steinke F., Muhlich P., Hamacher T., "Parametric study of variable renewable energy integration in Europe: Advantages and costs of transmission grid extensions", Energy Policy, Vol 42, 2012, pp. 498 – 508.*

[2] *Huang X.; Wang K.; Li.G., "Virtual Inertia Based Control of Two-stage Photovoltaic Inverters for Frequency Regulation in Islanded Micro-grid", IEEE Power & Energy Society General Meeting (PESGM), 2018.*

[3] *Moshari V., "Effects of the DC-DC converter's control and MPPT on synthetic inertia for double-stage PV systems".*

[4] *YongLi Z., JianGuo Y., Di W., "Comparative study of two stages and single-stage topologies for Grid-Tie Photovoltaic Generation by PSCAD/EMTDC", 2011The International Conference on Advanced Power System Automation and Protection, pp. 1304-1309, 2011.*

[5] A. Bolzoni, *"Advanced Control Strategies for Power Converters in AC Microgrids".*

[6] *D. Sera, L. Mathe, T. Kerekes, S. V. Spataru and R. Teodorescu, "On the Perturb-and-Observe and Incremental Conductance MPPT Methods for PV Systems," in IEEE Journal of Photovoltaics, vol. 3, no. 3, pp. 1070-1078, July 2013.*

[7] *Gupta A.K.; Saxena R. "Review on widely-used MPPT techniques for PV applications", International Conference on Innovation and Challenges in Cyber Security (ICICCS-INBUSH), India, February 2016, pp. 270–273.*

[8] Marconato R., *Electric Power Systems, Vol. 2.*

[9] Venkatramanan D., Vinod J., *"Dynamic Modeling and Analysis of Buck Converter Based Solar PV Charge Controller for Improved MPPT Performance", IEEE Trans. on Industry Applications, Vol. 55, Issue 6, Nov.-Dec. 2019, Vol. 55, pp. 6234 - 6246..*

[10] *Pokharel M., Ghosh A., Ho C. N. M., "Small-Signal Modelling and Design Validation of PV-Controllers With INC-MPPT Using CHIL", IEEE Trans. on Energy Conv., Vol. 34, Issue 1, March 2019, pp. 361 – 371..*

[11] *Bolzoni A., Terlizzi C., Perini R., "Analytical Design and Modelling of Power Converters*

Equipped with Synthetic Inertia Control", 2018 20th European Conf. on Power Electronics and Applications (EPE'18 ECCE Europe), 2018, pp. 1-9.

[12] Terna, *Regolazione Tecnica dei Requisiti di Sistema della Generazione Distribuita.*

A. Appendix A

For the calculation of equation (2.12), referring to [9] the voltage-current relation for the single-diode PV model is:

$$I_{pv} = I_{ph} - I_d - \left(\frac{V_{pv} + I_{pv}R_s}{R_{sh}}\right) \tag{A.1}$$

$$I_d = I_s\left[exp\left(\frac{V_{pv} + I_{pv}R_s}{\eta n_c V_t}\right) - 1\right] \qquad \rightarrow I_s exp\left(\frac{V_{pv} + I_{pv}R_s}{\eta n_c V_t}\right) = (I_d + I_s) \tag{A.2}$$

R_{pv_eq} can be found by derivation of (A.1):

$$\frac{\partial i_{pv}}{\partial v_{pv}} = -\frac{1}{R_{pv\_eq}} \tag{A.3}$$

Assuming I_{ph} and I_s as constants:

$$\frac{\partial i_{pv}}{\partial v_{pv}} = \frac{-I_s\left(1 + R_s\frac{\partial i_{pv}}{\partial v_{pv}}\right)exp\left(\frac{v_{pv} + i_{pv}R_s}{\eta n_c V_t}\right)}{\eta n_c V_t} - \frac{1}{R_{sh}} - \frac{R_s}{R_{sh}}\frac{\partial i_{pv}}{\partial v_{pv}} \tag{A.4}$$

Re-write the equation factoring out $\partial i_{pv}/\partial v_{pv}$ on the left-hand side:

$$\frac{\partial i_{pv}}{\partial v_{pv}}\left(1 + \frac{R_s}{R_{sh}} + \frac{R_s I_s exp\left(\frac{v_{pv} + i_{pv}R_s}{\eta n_c V_t}\right)}{\eta n_c V_t}\right) = \frac{-I_s exp\left(\frac{v_{pv} + i_{pv}R_s}{\eta n_c V_t}\right)}{\eta n_c V_t} - \frac{1}{R_{sh}} \tag{A.5}$$

Isolating $\partial i_{pv}/\partial v_{pv}$:

$$\frac{\partial i_{pv}}{\partial v_{pv}} = \frac{\dfrac{-I_s exp\left(\dfrac{v_{pv}+i_{pv}R_s}{\eta n_c V_t}\right)}{\eta n_c V_t} - \dfrac{1}{R_{sh}}}{1+\dfrac{R_s}{R_{sh}}+\dfrac{R_s I_s}{\eta n_c V_t} exp\left(\dfrac{v_{pv}+i_{pv}R_s}{\eta n_c V_t}\right)} \tag{A.6}$$

Considering (A.2):

$$\frac{\partial i_{pv}}{\partial v_{pv}} = \frac{\dfrac{-(I_s+I_d)}{\eta n_c V_t} - \dfrac{1}{R_{sh}}}{1+\dfrac{R_s}{R_{sh}}+\dfrac{R_s(I_s+I_d)}{\eta n_c V_t}} = \frac{-[R_{sh}(I_s+I_d)+\eta n_c V_t]}{R_s R_{sh}(I_s+I_d)+\eta n_c V_t(R_s+R_{sh})} \tag{A.7}$$

And finally, considering (A.3):

$$\begin{aligned} R_{pv\_eq} &= \frac{R_s[\eta n_c V_t + R_{sh}(I_s+I_d)]+R_{sh}\eta n_c V_t}{[R_{sh}(I_s+I_d)+\eta n_c V_t]} = \frac{R_{sh}\eta n_c V_t}{[R_{sh}(I_s+I_d)+\eta n_c V_t]} + R_s \\ &= \frac{\eta n_c V_t}{(I_s+I_d)} + R_{sh} + R_s = \left(\frac{I_s+I_d}{\eta n_c V_t}+\frac{1}{R_{sh}}\right)^{-1} + R_s \end{aligned} \tag{A.8}$$

B. Appendix B

This appendix includes the steps to derive the expression of K_m [10]. Starting from equation (3.34):

$$e = \frac{1}{v_{pv}} \cdot \frac{dp_{pv}}{dv_{pv}} = \frac{i_{pv}}{v_{pv}} + \frac{di_{pv}}{dv_{pv}} \tag{B.1}$$

The V-I characteristic of a PV source can be linearized as a straight-line tangent to the MPP of coordinates (V_{mpp}, I_{mpp}) as shown in Figure B.1:

$$(i_{pv} - I_{mpp}) = -\frac{1}{R_{mpp}} \cdot (v_{pv} - V_{mpp}) \tag{B.2}$$

Where R_{mpp} is the equivalent resistance of the PV source at MPP

The expression in (3.35) can be obtained by applying Taylor series expansion to (3.34) around the operating point (V_{mpp}, I_{mpp}) :

$$\begin{aligned} e(v_{pv}, i_{pv}) = e(V_{mpp}, I_{mpp}) &+ \left.\frac{\delta e(v_{pv}, i_{pv})}{\delta v_{pv}}\right|_{(V_{mpp}, I_{mpp})} \cdot (v_{pv} - V_{mpp}) \\ &+ \left.\frac{\delta e(v_{pv}, i_{pv})}{\delta i_{pv}}\right|_{(V_{mpp}, I_{mpp})} \cdot (i_{pv} - I_{mpp}) \end{aligned} \tag{B.3}$$

$$e(v_{pv}, i_{pv}) = -\frac{I_{mpp}}{{V_{mpp}}^2} \cdot (v_{pv} - V_{mpp}) + \frac{1}{{V_{mpp}}^2} \cdot (i_{pv} - I_{mpp}) \tag{B.4}$$

Substituting the expression from (B.2) into (B.4), it results:

$$e = \frac{2}{R_{mpp}} - \frac{2v_{pv}}{R_{mpp}V_{mpp}} \tag{B.5}$$

Introducing small-signal perturbation, (B.5) can be expressed as:

$$\bar{e} = -\frac{2}{R_{mpp}V_{mpp}} \bar{v}_{pv} \tag{B.6}$$

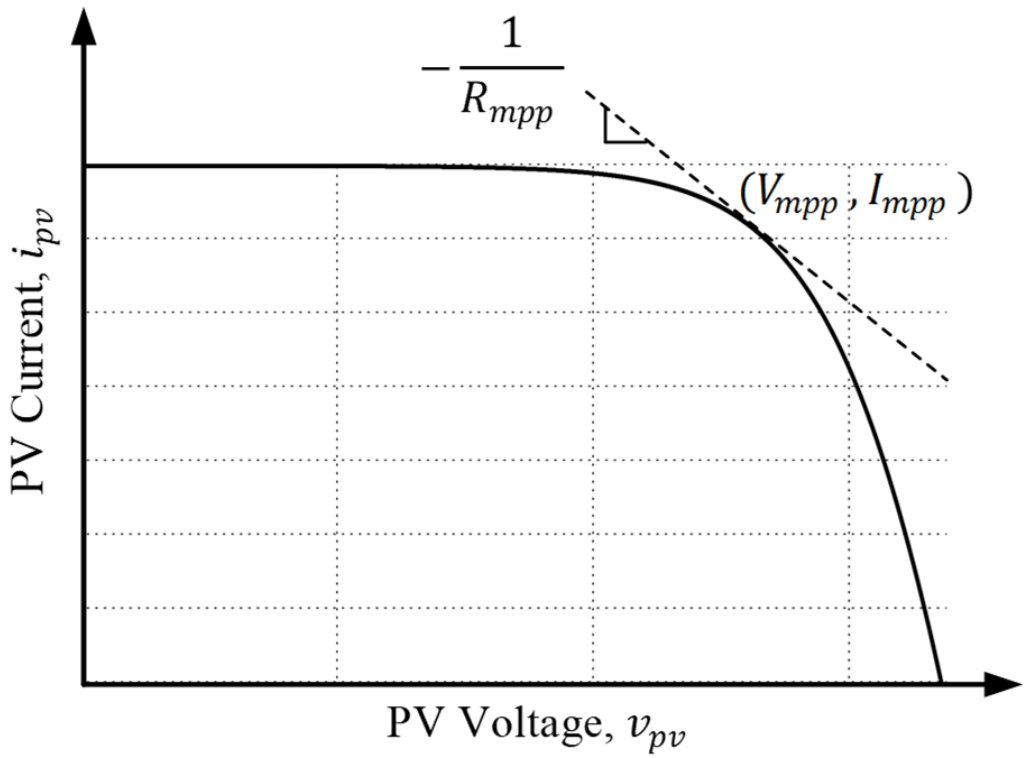

Figure B.1 – PV source V-I characteristic linearized around the MPP [10].

List of Figures

List of Tables